Theses and Dissertations   Student Graduate Works

3-22-2019

Source Term Estimation of Atmospheric Pollutants Using an Ensemble of HYSPLIT Concentration Simulations

Casey L. Zoellick

Follow this and additional works at: https://scholar.afit.edu/etd

Part of the Atmospheric Sciences Commons, and the Nuclear Commons

Source Term Estimation of Atmospheric
Pollutants Using an Ensemble of HYSPLIT
Concentration Simulations

THESIS

Casey L. Zoellick, Captain, USAF

AFIT-ENP-MS-19-M-096

DEPARTMENT OF THE AIR FORCE
AIR UNIVERSITY

AIR FORCE INSTITUTE OF TECHNOLOGY

Wright-Patterson Air Force Base, Ohio

AFIT-ENP-MS-19-M-096

SOURCE TERM ESTIMATION OF ATMOSPHERIC POLLUTANTS

USING AN ENSEMBLE OF HYSPLIT CONCENTRATION SIMULATIONS

THESIS

Presented to the Faculty

Department of Engineering Physics

Graduate School of Engineering and Management

Air Force Institute of Technology

Air University

Air Education and Training Command

in Partial Fulfillment of the Requirements for the

Degree of Master of Science in Atmospheric Science

Casey L. Zoellick, B.S.

Captain, USAF

21 March 2019

DISTRIBUTION STATEMENT A

AFIT-ENP-MS-19-M-096

SOURCE TERM ESTIMATION OF ATMOSPHERIC POLLUTANTS

USING AN ENSEMBLE OF HYSPLIT CONCENTRATION SIMULATIONS

THESIS

Casey L. Zoellick, B.S.
Captain, USAF

Committee Membership:

Maj H.R. Tseng, Ph.D.
Chair

Lt Col R. Tournay, Ph.D.
Member

Dr. A. Suarez-Mullens, Ph.D.
Member

AFIT-ENP-MS-19-M-096

Abstract

In support of Comprehensive Nuclear-Test-Ban Treaty (CTBT) monitoring and nuclear event detection, this study works toward source term estimation (STE) of dispersive pollutants using a novel method—an ensemble of forward trajectory concentration simulations using a meteorology-coupled dispersion model. Traditionally a mathematically and physically rigorous problem, STE of a plume of atmospheric pollutants can be solved in a variety of ways depending on what is known regarding the emission, but little has been studied on the sensitivity between the horizontal resolution of the meteorology data in relation to the dispersion model and the results derived from known concentrations at multiple locations. This study tackles both these issues of resolution and observation sensitivities by employing the Hybrid Single Particle Lagrangian Integrated Trajectory (HYSPLIT) model, coupled with data from the 1983 Cross-Appalachian Tracer Experiment (CAPTEX), to determine the location of the experimental tracer releases. This is accomplished by conducting an ensemble of HYSPLIT forward concentration simulations using a grid of first-guess locations and storing the model-derived concentration values in a source-receptor matrix (SRM). The model rank for each simulation is calculated using ground measurements, and the location yielding the highest model rank is determined to be the source. Simultaneously, this study produces information regarding source-receptor relationships to terrain features. Furthermore, the study then applies the SRM methodology to locate the detonation location of two nuclear tests conducted in the 1950s at the Nevada Test Site (NTS). Knowing the sensitivity of the STE solution based on the number of available measurements is useful for determining the location of a release of radionuclides into the atmosphere in support of nuclear treaty monitoring.

iv

Acknowledgements

Table of Contents

List of Figures

List of Tables

List of Acronyms

AGL above ground level

ARL Air Resources Laboratory

Bq Becquerel

CAPTEX Cross-Appalachian Tracer Experiment

CDF cumulative distribution function

CTBT Comprehensive Nuclear-Test-Ban Treaty

DATEM Data Archive of Tracer Experiments and Meteorology

DoD Department of Defense

ESRL Earth System Research Laboratory

FB fractional bias

FMS figure of merit in space

FORTRAN Formula Translation

HPC high performance computing

HYSPLIT Hybrid Single Particle Lagrangian Integrated Trajectory

ICHEM in-line chemical conversion module

KS Kolomogorov-Smirnov

kT kiloton

kts knots

METREX Metropolitan Tracer Experiment

MYNN Mellor-Yamada-Nakanishi-Niino

NARR North American Regional Reanalysis

NCAR National Center for Atmospheric Research

NCEP National Centers for Environmental Prediction

NOAA National Oceanic and Atmospheric Administration

NTS Nevada Test Site

NUDET nuclear detonation

NWS National Weather Service

OH Ohio

ON Ontario

PBL planetary boundary layer

PMCH perfluoro-monomethyl-cyclohexane

R correlation coefficient

rem Roentgen equivalent man

SRM source-receptor matrix

STE source term estimation

TKE turbulent kinetic energy

U-235 uranium-235

USAF United States Air Force

UTC Coordinated Universal Time

WRF Weather Research and Forecasting

YSU Yonsei University

SOURCE TERM ESTIMATION OF ATMOSPHERIC POLLUTANTS

USING AN ENSEMBLE OF HYSPLIT CONCENTRATION SIMULATIONS

I. Introduction

Motivation

Determining the origination aspects of atmospheric pollutants appeals to a variety
of applications and users. The method of obtaining a source term estimation (STE)
depends on which combination of factors are needed for the application: the time of
the pollutant release, the location of the pollutant release, and the amount of pollutant
released. These methods fall into three categories: direct forward modeling, direct
backward or inverse modeling, and nonlinear optimization approaches (Bieringer et al.
2017).

Direct forward methods involve simulating the atmospheric transport and disper-
sion physics in the positive time dimension. This is generally advantageous when the
location and time of the source term are known in addition to downstream concen-
tration measurements, and the user is determining the amount or rate of pollutant
released into the atmosphere (Bieringer et al. 2017). The dispersion model can es-
tablish a source-receptor relationship between the known source and concentration
observations, and the pollutant release rate can be fine-tuned to optimize this re-
lationship to match the observations (Seibert and Frank 2004). The sensitivity of
this relationship to specific observations can also be investigated. This type of anal-
ysis is important in chemical and radiological release situations where public safety
is paramount, and the rate of pollutant release helps determines if and how many

people need to evacuate the affected area.

Forward dispersion models can also be utilized in nonlinear optimization approaches when uncertainty exists in the source location. This source-oriented method entails running the forward dispersion model many times over the likely source domain and adjusting the model configuration to match the predicted concentration values to the observed concentration values. These adjustments can be determined from Bayesian updating and interference methods by using stochastic Monte Carlo sampling (Shankar Rao 2007). This method attempts to search for the set of parameters that maximize the skill of the forward dispersion simulation and minimize the error (Bieringer et al. 2017). This method can be computationally intensive because a simulation needs to be conducted for each source being tested. Assigning a separate species to each source and tracking each species independently throughout one model run saves computational expense; however, this is not possible in more complex simulations where multiple species are required for each source in order to accurately simulate the dispersion phenomenon (Seibert and Frank 2004).

The last method, the inverse or backward method, involves running the model backward from known concentration observations or receptors to determine the source term. This method entails running parcel trajectories from the receptors to determine the source of that particular air parcel (Bieringer et al. 2017). This receptor-oriented approach is more computationally efficient than forward methods when the number of sources outnumbers the receptors (Shankar Rao 2007). Applications where the attributes of the source are unknown benefit from the efficiency of the inverse method to narrow down a source region or the number of sources. However, this methodology is not appropriate for determining release rates or precise location estimates (Bieringer et al. 2017).

One defense application of STE techniques is nuclear treaty monitoring. The

Comprehensive Nuclear-Test-Ban Treaty (CTBT) bans nuclear tests in any environment in the atmosphere, underwater, and underground (Bieringer et al. 2017). All three STE approaches previously mention can be employed to ensure signatory countries abide by the treaty. This ensures that when nuclear fission byproducts are detected, their source can be determined and appropriate actions taken against the offending country.

This study proposes a methodology utilizing an ensemble of forward dispersion model simulations by varying the source location to determine which sources maximize the performance metrics of the model when compared to the observational dataset. While techniques involving forward concentrations simulations have been studied in the past, little is known regarding the sensitivity of the horizontal resolution of the meteorological data in relation to the dispersion model and the results derived from the observed concentration values. Therefore, this study tests the sensitivity of the configuration of these ensembles in order to optimize the methodology under different meteorological conditions while conserving computational expense. This methodology is source-oriented, and is advantageous when determining one source location given a number of concentration observations. The case of CTBT monitoring fits this description as multiple observations of radioactive contaminants downstream of a test or release can be utilized to determine the origination location.

Preview

The rest of this study is organized into four chapters. Chapter II discusses the background of atmospheric transport and dispersion modeling, introduces the Hybrid Single Particle Lagrangian Integrated Trajectory (HYSPLIT) model, and explains its simulation of transport, dispersion, and deposition in the atmosphere. The Cross-Appalachian Tracer Experiment (CAPTEX) and stabilized nuclear clouds are

3

also described in order to provide data on which to test the methodology of this study.

Chapter III describes the methodology and how HYSPLIT is configured in order to conduct the sensitivity analyses and illustrates the concept of a source-receptor matrix (SRM), which serves as the main data structure for the ensemble simulations. The temporal and spatial sensitivity tests of the STE solutions to the observations are explained as well. The chapter concludes by discussing how the methodology extends to determining the source location of nuclear tests conducted from 1951 to 1957.

Next, Chapter IV presents the results and analyses of the tests described in Chapter III. The sensitivity results of the SRM configurations are discussed with the CAPTEX data. The sensitivity results of the SRM configurations applied to the CAPTEX releases shape how the methodology is utilized during the nuclear test ensembles. The performance of this methodology on the nuclear test cases is also analyzed.

Lastly, Chapter V presents conclusions regarding the temporal and spatial sensitivity analyses of the CAPTEX data tests in the context of user applications and optimizing the performance of the methodology under computational and meteorological condition constraints. Proposed future work includes analyzing other sensitivities of the STE solution and incorporating machine learning techniques, which can further improve the execution of this methodology within HYSPLIT.

II. Background

Atmospheric Transport and Dispersion Modeling

Atmospheric transport and dispersion of particles or gases primarily rely on three meteorological processes. First, contaminants are transported away from their source location by the mean wind velocity field (Samson 1988). As the plume moves away from the point of emission, it is dispersed and expanded by smaller-scale turbulent processes occurring within the mean wind flow (Samson 1988). Finally, particles can undergo wet deposition processes such as in-cloud scavenging and dry depositions processes such as gravitational settling and impaction (Samson 1988; Wesely 1989). Models vary on the parameterizations of these processes and the characterization of the aerosols themselves. Some categories of atmospheric transport and dispersion models include box models, Gaussian plume models, Lagrangian models, Eulerian dispersion models, and dense gas models (Hutchinson et al. 2017).

Despite these varied approaches, most atmospheric dispersion models tend to numerically solve for the time evolution of air contaminant concentrations with Lagrangian and Eulerian approaches (Draxler and Hess 1998). The Eulerian methodology uses a fixed three-dimensional grid of reference to compute the pollutant concentrations. On the other hand, the Lagrangian method uses a moving frame of reference to follow the trajectories of the air parcels while performing the advection and diffusion calculations (Stein et al. 2015). The atmospheric emission scenario often dictates which framework is more advantageous, and thus, can contribute to a user choosing one model over another.

Eulerian methods are best utilized for complex emission scenarios, which require solutions at all grid points (Draxler and Hess 1998). Examples include cases requiring concentrations at multiple locations and contaminants sourced from multiple locations
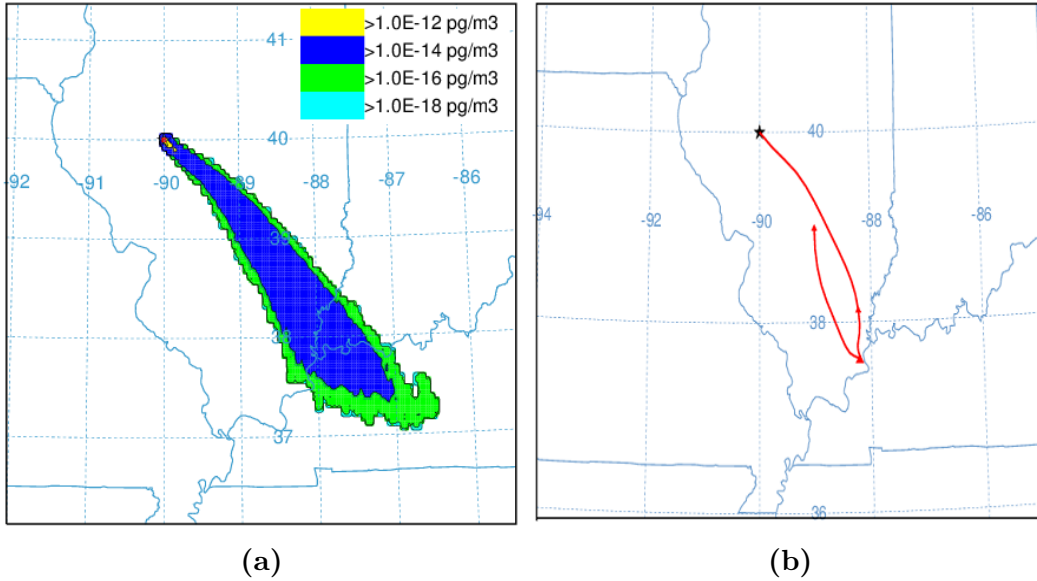
Figure 1. Concentrations shown across the grid in (a) portray the Eulerian perspective, while a single trajectory in (b) shows the Lagrangian perspective.

and times. Thus, emissions must be defined on the same scale that the model is using to perform the calculations (Draxler and Hess 1998).

In contrast, Lagrangian techniques are advantageous for single-source emission scenarios in which the computation is restricted to only neighboring grid points (Draxler and Hess 1998). Examples include gas leaks, smoke, and volcanic ash where the trajectory of the pollutants is more important than explicit concentration values where the emission can be traced back to one point in space and time. This means that Lagrangian models can define emission at any resolution (Draxler and Hess 1998). Figure 1 shows the difference between a concentration plume (Eulerian perspective) and simple trajectory (Lagrangian perspective).

The HYSPLIT Model

Developed by the National Oceanic and Atmospheric Administration (NOAA) Air Resources Laboratory (ARL), the HYSPLIT model combines the Eulerian and Lagrangian approaches. The advection and diffusion calculations are made in the

Lagrangian frame of reference while the pollutant concentrations are computed on a fixed grid, which is the Eulerian frame of reference (Draxler and Hess 1998). In this way, HYSPLIT takes advantage of both approaches and employs one method where the other is disadvantageous.

The HYSPLIT lineage can be traced back to trajectory calculations accomplished by hand. When reconnaissance aircraft detected radioactive fallout over the Kamchatka Peninsula in the Soviet Union suspected to be from an atomic test, the United States Weather Bureau, the National Weather Service (NWS) predecessor, was tasked with determining its source (Stein et al. 2015). These calculations were performed by hand using the geostrophic wind assumption that the mid-tropospheric winds followed the 500-hPa height contours measured by weather balloons. Since this event, trajectory calculations have been a primary focus of research at ARL, and HYSPLIT was developed in support of this research (Stein et al. 2015). In the early 1980s, the first version of HYSPLIT was released utilizing solely rawinsonde observations with dispersion due to uniform mixing during the daytime and no mixing during nighttime (Draxler and Hess 2018). Each night, the daytime mixed layer was split into layers to replicate dispersion due to nocturnal wind shear (Draxler and Hess 1998). The second version of HYSPLIT interpolated the rawinsonde and other observed data to estimate the vertical mixing coefficients, which vary in space and time (Stein et al. 2015). It was not until the third version that gridded meteorological analyses and forecasts from standard numerical weather models were able to be incorporated into HYSPLIT (Draxler and Hess 2018). A follow-on study concluded that HYSPLIT was just as accurate using meteorological model data as observed rawinsonde data, even with an increase in temporal resolution of the rawinsonde data included in the calculations (Draxler and Hess 1998). Currently, HYSPLIT is operational on its fourth version, which is the focus of the remainder of this section and is the version utilized
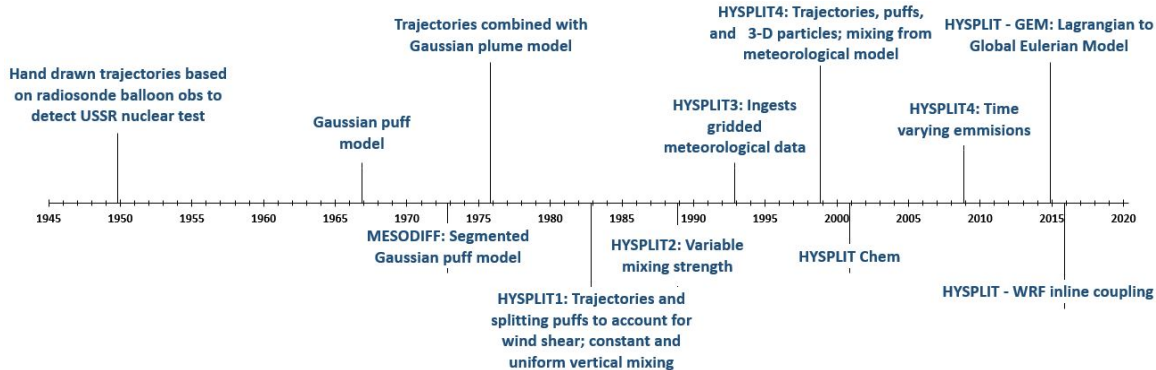
Figure 2. Milestones in the HYSPLIT development, including initial advances in atmospheric transport and dispersion modeling (Stein et al. 2015).

in this study. Figure 2 shows the history of the development of HYSPLIT and the beginnings of atmospheric transport and dispersion modeling that predate it.

Data Assimilation and Grids

The HYSPLIT grid is determined by the grid of the meteorological data that is ingested into the model; however, this data requires specific preprocessing in order for HYSPLIT to use it. While most meteorological models use some variation of a terrain-following (σ) coordinate system, their outputs are usually interpolated to a variety of different vertical coordinate systems (Draxler and Hess 2018). To maintain flexibility with data ingest, HYSPLIT linearly interpolates the profiles of the meteorological data at each horizontal grid point to its internal terrain-following system:

$$\sigma = 1 - \frac{z}{z_{top}}, \tag{1}$$

where z is the height relative to the terrain and z_{top} is the top of the HYSPLIT coordinate system (Draxler and Hess 1998). HYSPLIT applies this conversion to data on pressure-sigma, pressure-absolute, terrain-sigma, and hybrid absolute-pressure-sigma vertical coordinate systems (Draxler and Hess 2018).

HYSPLIT supports three map projections: Polar Stereographic, Mercator, and
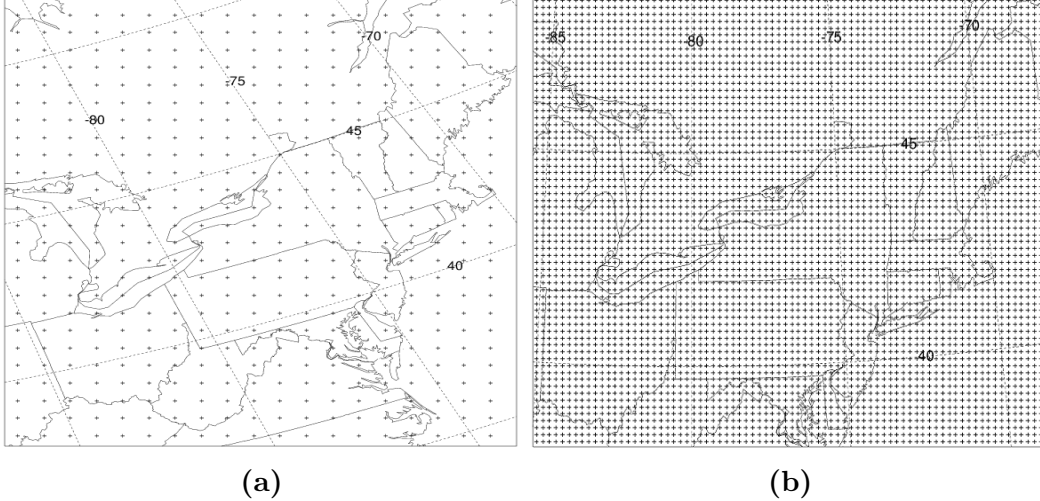
Figure 3. Two examples of grids ingested into HYSPLIT. The North American Regional Reanalysis (NARR) with 27-km resolution is shown in (a), and the Weather Research and Forecasting (WRF) model with 9-km resolution is shown in (b).

Lambert Conformal. A simulation may contain multiple meteorological files with different grids on different map projections, and HYSPLIT converts each of them (Draxler and Hess 1998). Figure 3 shows two examples of meteorological grids that have been preprocessed by HYSPLIT. Higher resolution is required for precise concentration levels near the source region, but as the plume expands with time and distance, coarser resolution is adequate and saves computational expense, as HYSPLIT dynamically adjusts the integration time step based on the grid resolution (Air Resources Laboratory 2018a). This is determined from the relationship:

$$U_{max}\Delta t < 0.75, \tag{2}$$

where U_{max} is the maximum transport velocity from the previous hour in grid-units per minute, and Δt is the dynamic time step in minutes whose product cannot exceed 0.75 grid-units (Draxler and Hess 2018). HYSPLIT automatically chooses the grid to perform the calculations on either the meteorological data grid or a user-defined grid, generally whichever is finer (Air Resources Laboratory 2018a). Indeed, one of

9

the strengths of HYSPLIT is its flexibility to accomplish the transport and dispersion calculations on multiple meteorological model grids. However, HYSPLIT is disadvantaged in that its plume forecast is only as accurate as the meteorological data that it ingests. Any error in the weather forecast will propagate in the HYSPLIT forecast.

Transport and Advection

The most fundamental feature of HYSPLIT is the advection equation it uses to calculate the atmospheric transport of the emitted puffs or particles (Dispersion and Concentration subsection below). This is analogous to the dynamic core of traditional meteorological models: HYSPLIT is explicitly solving for the position of the particle or puff as it transits across the grid. It solves for the final position, $P(t+\Delta t)$, by using the three-dimensional average of the velocity vector, $\mathbf{V}$, at the initial and first-guess position of the particle (Stein et al. 2015). The first-guess position, $P'(t + \Delta t)$, is calculated by:

$$P'(t + \Delta t) = P(t) + \mathbf{V}(P,t)\Delta t, \tag{3}$$

where $P(t)$ is the initial position of the particle, $\mathbf{V}(P,t)$ is the velocity vector at the initial position, and Δt is the time step (Draxler and Hess 1998). The velocity at the first-guess position is then used in the final position calculation:

$$P(t + \Delta t) = P(t) + \frac{1}{2}[\mathbf{V}(P,t) + \mathbf{V}(P',t + \Delta t)]\Delta t, \tag{4}$$

where $\mathbf{V}(P',t+\Delta t)$ is the velocity vector at the first-guess position (Draxler and Hess 1998). These are the only equations considered during trajectory calculations. The trajectory is terminated if it intersects the top of the model, which is user-adjustable, and advection will continue along the ground if the trajectory intersects the surface (Draxler and Hess 2018). Because the meteorological data is linearly interpolated

to the HYSPLIT internal grid, higher order versions of this equation do not yield better results even though they are more computationally expensive (Draxler and Hess 1998). As previously discussed, Δt varies during the simulation as HYSPLIT optimizes the integration time step based on the grid size and maximum particle advection speed.

Dispersion and Concentration

Lagrangian models like HYSPLIT can treat the emission either as a series of puffs with each containing a fraction of the overall mass of the pollutant, or as a release of many particles over the course of the simulation (Draxler and Hess 1998). When HYSPLIT treats the emission as puffs in the horizontal dimensions, it splits the puffs when they exceed the size of a grid space (Draxler and Hess 1998). Grid-scale processes are thus simulated by the puff-splitting process while sub-grid processes are modeled by the turbulent dispersion parameterizations (Draxler and Hess 1998). In this way HYSPLIT calculates concentrations on grid spaces based on the fractional mass of the puff it contains. In the vertical dimension, treating pollutants as particles captures the inhomogeneity of the vertical structure of the atmosphere (Draxler and Hess 1998). This also limits the amount of puffs HYSPLIT is required to track and decreases simulation run times (Air Resources Laboratory 2018a).

Capturing the vertical structure and stability of the atmosphere is essential to obtaining an accurate dispersion calculation, especially when the pollutants interact with the planetary boundary layer (PBL). Vertical mixing is parameterized in HYSPLIT four ways. The most preferred method is to use the fluxes of heat and momentum prescribed from the gridded meteorological data, giving solutions that are representative of the meteorological conditions prescribed in the meteorological data (Draxler and Hess 1998). However, when the meteorological data lack the heat

11

and momentum fluxes, HYSPLIT has the flexibility to assume that the mixing diffusivities follow the coefficients for heat, derive the mixing from the horizontal and vertical frictional velocities and the PBL height, or use the turbulent kinetic energy (TKE) fields in case the gridded meteorological data is missing the pertinent vertical motion variables (Stein et al. 2015).

In both the particle and puff treatment of the contaminant, dispersion is parameterized by adding a turbulent component onto the mean velocity from the meteorological data (Draxler and Hess 2018). In the case of the particle model, the final position incorporates the turbulent component. Equation 5 shows the final position, P_{final}, after the turbulent component, $\mathbf{V}'$, is added to position that was calculated by the mean flow, P_{mean} (Air Resources Laboratory 2018a):

$$P_{final}(t + \Delta t) = P_{mean}(t + \Delta t) + \mathbf{V}'(t + \Delta t)\Delta t. \tag{5}$$

The turbulent component is determined from the turbulent component of the previous time step, an auto-correlation coefficient, R_a, and the Lagrangian time scale, T_{Li}:

$$\mathbf{V}'(t + \Delta t) = R_a(\Delta t)\mathbf{V}'(t) + \mathbf{V}''(1 - R_a(\Delta t)^2)^{\frac{1}{2}}, \tag{6}$$

where

$$R_a(\Delta t) = \exp\left(\frac{-\Delta t}{T_{Li}}\right), \tag{7}$$

and $\mathbf{V}''$ is the Gaussian random component, which is derived from a computer-generated random number and the standard deviation of the velocity, σ_V (Air Resources Laboratory 2018a).

Horizontal dispersion for the puff model is parameterized by the puff growth rate when the standard deviation of the horizontal distribution of the puff, σ_h, is smaller than the grid size. The standard deviation of the velocity from above defines this

growth rate (Air Resources Laboratory 2018a):

$$\frac{d\sigma_h}{dt} = \sigma_V. \tag{8}$$

When the horizontal puff size is larger than the grid spacing and is split, the model actually resolves the dispersion explicitly (Draxler and Hess 1998). The method for splitting the puff depends on whether the user chooses to model a Top-Hat-distributed or Gaussian-distributed puff. Figure 4 shows a cross-section of how the concentration of mass is distributed about the axis of the mean trajectory of each type of puff. A Top-Hat-distributed puff assumes a uniform concentration within 1.5 standard deviations (σ) of the center with zero concentration outside and is split into four equal puffs, each with 25% of the original mass of the puff (Draxler and Hess 2018). A Gaussian-distributed puff assumes a normal distribution of concentration about the center over 3σ and is split into five new puffs with the center puff receiving 60% of the original mass and the four outside puffs each receiving 10% of the original mass (Air Resources Laboratory 2018a; Draxler and Hess 2018).

The concentration calculation differs depending on whether the particle, Top-Hat-distributed puff, or Gaussian-distributed puff is contained within the grid cell. Each calculation defines the increment concentration contribution, Δc, of each particle or puff. This is defined for a single particle of mass m in a 3-D grid space by:

$$\Delta c = \frac{m}{\Delta x \Delta y \Delta z}. \tag{9}$$

Next, the concentration contribution of a Top-Hat puff of mass m is defined by:

$$\Delta c = \frac{m}{(\pi r^2 \Delta z)}, \tag{10}$$
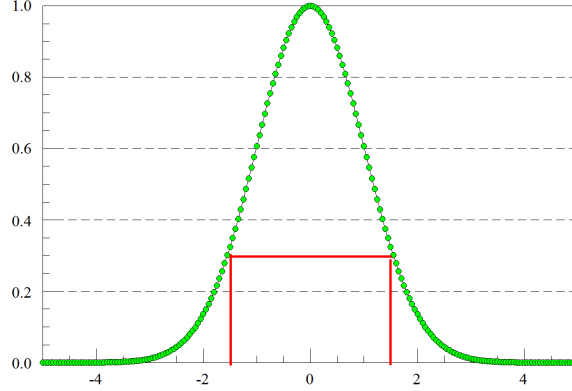
Figure 4. The concentration distribution about the axis of the mean trajectory for a Top-Hat-distributed (red) and a Gaussian-distributed (green) puff. The vertical axis is the density function, and the horizontal axis is the number of σ (Air Resources Laboratory 2018a).

where the radius r is $1.54\sigma_h$ and the vertical extent Δz is $3.08\sigma_z$ (σ_z being standard deviation of the vertical distribution of the puff) (Draxler and Hess 2018). Finally, the incremental concentration contribution of a Gaussian puff is:

$$\Delta c = \frac{m}{2\pi\sigma_h^2\Delta z}\exp\left(\frac{-0.5x^2}{\sigma_h^2}\right), \tag{11}$$

where x is the distance from the center of the puff to the grid node and all other terms are the same as previously defined (Draxler and Hess 2018). Figure 5 shows how a Gaussian puff is distributed in three dimensions. The user can use either the particle, Top-Hat puff, or Gaussian puff parameterizations in any combination for the vertical and horizontal dimensions. Pure particle simulations quickly become computationally expensive, and puffs generally do not capture the vertical structure of the atmosphere accurately; so a common application is to use a particle parameterization in the vertical, and one of the two puff parameterizations in the horizontal (Air Resources Laboratory 2018a).

14
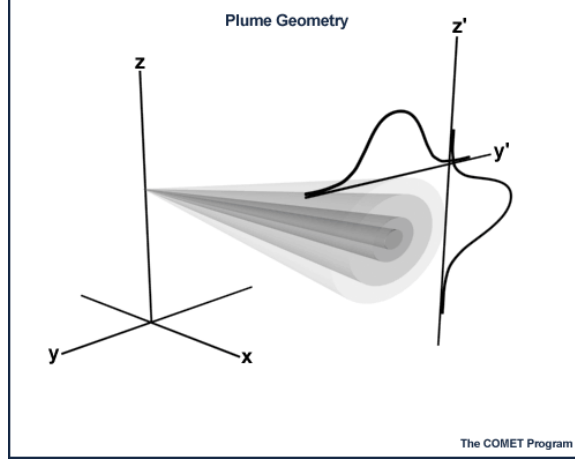
Figure 5. Three-dimensional view of a Gaussian-distributed plume advecting along the x-axis. The mass is distributed normally about the x-axis in the y and z directions (Spangler 2002).

Deposition

Aerosols or gases are removed from the pollutant plume by dry deposition, wet deposition, and radioactive decay (if the pollutants are radioactive) (Draxler and Hess 1998). The total deposition is the sum of the removal constants for the deposition processes. Dry deposition in HYSPLIT is triggered when the plume interacts with the surface layer, which is the second layer of meteorological data (Draxler and Hess 1998). The removal constant is:

$$\beta_{dry} = \frac{V_d}{\Delta Z_p},\qquad(12)$$

where V_d is the deposition velocity, and ΔZ_p is the depth of the pollutant layer, which is the surface layer for dry removal (Draxler and Hess 2018). V_d can be the gravitational settling velocity, explicitly defined by the user, or calculated by summing the resistances of the particles in the layer (Draxler and Hess 1998; Wesely 1989).

Wet deposition occurs when the pollutant particles mix with cloudy air, or when precipitation falls through the particles. Removal is computed using a scavenging

ratio, S_r, for in-cloud processes, and an average scavenging coefficient, S_c, for below-cloud processes (Draxler and Hess 1998). The constant for in-cloud removal is:

$$\beta_{inc} = \frac{F^t F_b S_r P_r}{\Delta Z_p},\tag{13}$$

where F^t is the fraction of the pollutant layer that is below the cloud top, F_b is the fraction of the pollutant layer that is above the cloud base, P_r is the precipitation rate, and the other variables are the same as previously defined (Draxler and Hess 1998). The constant for below-cloud removal is defined by (Draxler and Hess 1998):

$$\beta_{bel} = S_c(1 - F_b).\tag{14}$$

Wet deposition for gases is treated separately from wet deposition for particles. The deposition depends on gas solubility. For inert gases, this is a function of Henry's Law constant (H), which is the ratio of the equilibrium concentration of the gas in water to its concentration in air (Draxler and Hess 1998). Thus, the wet removal constant for gases is applied from the surface to the top of the cloud layer and is calculated as:

$$\beta_{gas} = \frac{F^t H R T P_r}{\Delta Z_p},\tag{15}$$

where R is the universal gas constant, T is the temperature, and all other variables are the same as above (Draxler and Hess 1998). Therefore, the total deposition is parameterized as follows:

$$D_{wet+dry} = m\{1 - \exp[-\Delta t(\beta_{dry} + \beta_{gas} + \beta_{inc} + \beta_{bel})]\},\tag{16}$$

where m is the mass of the pollutant particle or puff (Draxler and Hess 2018). While these equations are the basis for how HYSPLIT parameterizes deposition processes,

newer versions of the model also have an option to estimate the scavenging coefficient for in-cloud wet deposition (Stein et al. 2015). Deposition configurations used in this study are discussed in below.

Cross-Appalachian Tracer Experiment (CAPTEX)

The CAPTEX was a tracer experiment conducted across the eastern United States and southeastern Canada in September and October of 1983. The experiment consisted of seven releases of perfluoro-monomethyl-cyclohexane (PMCH), an inert gas with a low constituency in the atmosphere, which makes it easily detectable above the background level. The experiment aimed to test tracer technology on the 1000-km scale, to provide data to evaluate computer models, and to discover the mechanisms involved in long range transport and dispersion (Ferber et al. 1986). CAPTEX 1-4 and 6 were released from Dayton, Ohio (OH), and CAPTEX 5 and 7 were released from Sudbury, Ontario (ON), on the dates and at the times listed in Table 1. The Dayton releases occurred in the late afternoon to ensure vertical mixing of the tracer gas through the PBL, and the Sudbury releases started early in the morning behind cold fronts to ensure each of the tracer plumes was advected over the sampling network to the southeast (Ferber et al. 1986). The PMCH release occurred over three hours for all CAPTEX releases except for 6, which only persisted for 30 minutes.

The advantage to using CAPTEX data for this investigation is the robust sampling network—86 stations scattered across southern Canada and the northeastern United States between 280 km and 1200 km away from the release locations—as well as the various meteorological conditions under which the releases were executed. Figure 6 shows the locations of the sample sites relative to the three release locations. A detailed description of each sampling site is available in Table 16 in Appendix A. Samplers located closer to the release conducted 3-hour samples to capture more

	Release Date	Time (UTC)	Location	Duration (Hours)	Amount of PMCH Released (kg)
CAPTEX 1	18 Sept 1983	1700	Dayton, OH (39.80N, 84.05W)	3	208
CAPTEX 2	25 Sept 1983	1700	Dayton, OH (39.90N, 84.22W)	3	201
CAPTEX 3	02 Oct 1983	1900	Dayton, OH (39.90N, 84.22W)	3	201
CAPTEX 4	14 Oct 1983	1600	Dayton, OH (39.90N, 84.22W)	3	199
CAPTEX 5	26 Oct 1983	0400	Sudbury, ON (46.62N, 80.78W)	3	180
CAPTEX 6	28 Oct 1983	1530	Dayton, OH (39.90N, 84.22W)	0.5	32
CAPTEX 7	29 Oct 1983	0600	Sudbury, ON (46.62N, 80.78W)	3	183

Table 1. Information regarding each CAPTEX release date, time, location, duration, and amount of PMCH released (Ferber et al. 1986).
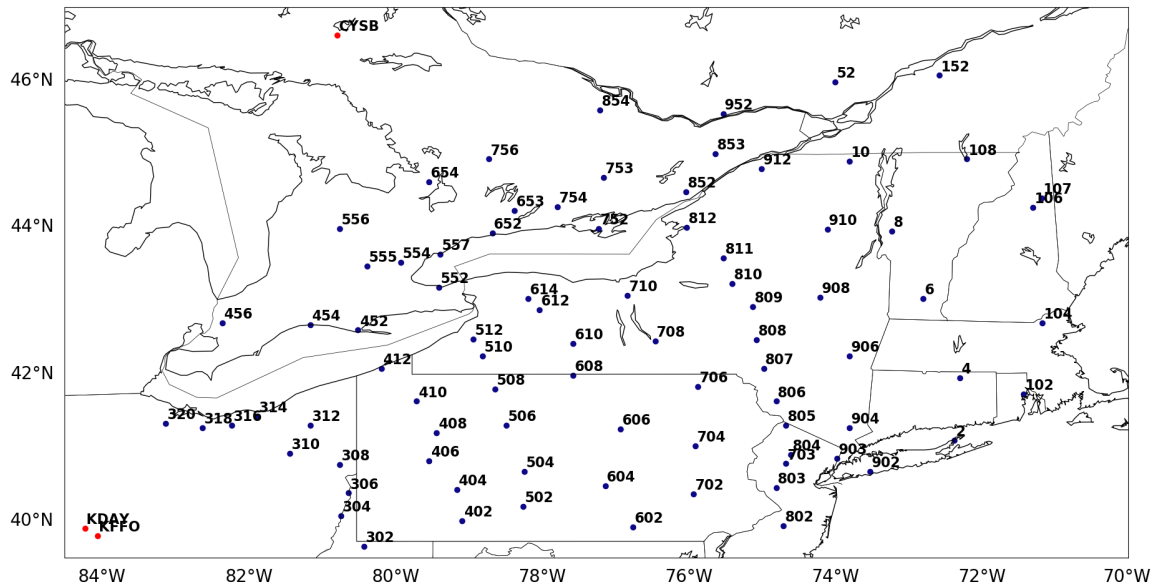
Figure 6. Location of sampling stations (numbered blue points) and release locations of Dayton, OH (KDAY and KFFO) and Sudbury, ON (CYSB) (red points). Location information derived from Ferber et al. (1986).

fidelity of the definition of the plume just following its release while sites farther away sampled for six hours. Sampling began prior to the release and continued for up to three days following. The goal was for each sampler to create a record that captured the arrival, peak, and departure of the tracer plume (Ferber et al. 1986). Thus, the observational record contains both null and positive concentration entries. This allows the STE methodology to compare not only how the model transports the plume through the network, but also ensures the model does not over-disperse the plume into regions it was not observed.

(a) CAPTEX 1 - 18 Sep 1800 UTC **(b) CAPTEX 2 - 25 Sep 1800 UTC**

(c) CAPTEX 3 - 2 Oct 1800 UTC **(d) CAPTEX 4 - 14 Oct 1500 UTC**

(e) CAPTEX 5 - 26 Oct 0300 UTC **(f) CAPTEX 7 - 29 Oct 0600 UTC**

925-hPa Geopotential Height (m)
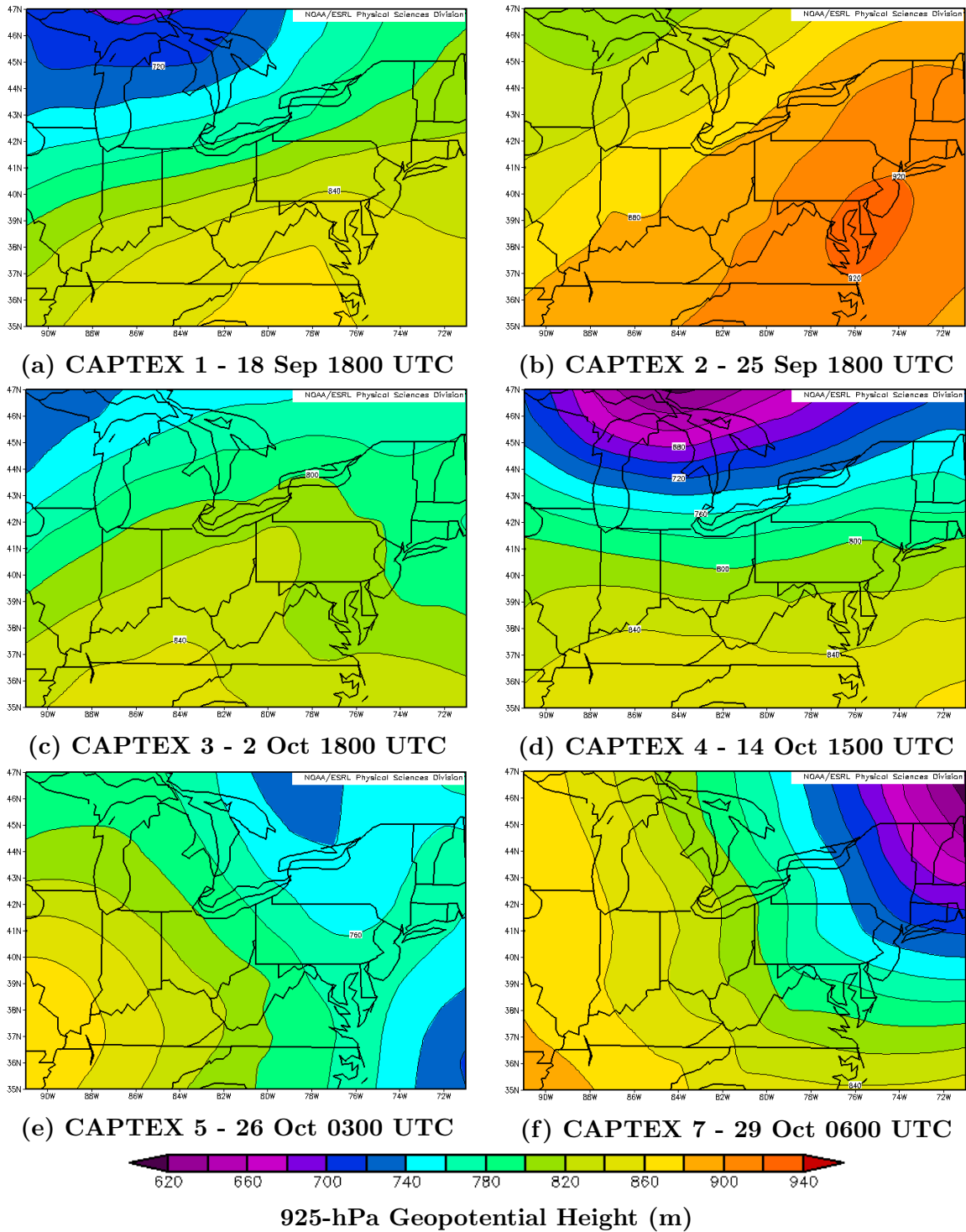
Figure 7. Geopotential heights of the 925-hPa atmospheric layer within the PBL from the NARR dataset over the CAPTEX domain. Charts are valid at the times shown, which are the nearest available data to the actual release times.

Available meteorological data are from the North American Regional Reanalysis (NARR) and Weather Research and Forecasting (WRF) model, and are both utilized in this study. The NARR is 32.5-km resolution and does not prescribe heat and momentum fluxes, thus, HYSPLIT defaults to solving them by using the wind and temperature profiles. The first WRF dataset is obtained from Ngan and Stein (2017) and includes 27 and 9-km resolutions created with version 3.5.1 of the model. The second WRF dataset is from the HYSPLIT Tutorial created with an older version of WRF. This is available in 27-km, 9-km, and 3-km resolutions for the CAPTEX 2 release only. The main difference between two sets of WRF parameterizations is the Ngan and Stein (2017) data utilized the Mellor-Yamada-Nakanishi-Niino (MYNN) PBL scheme while the HYSPLIT Tutorial data used the Yonsei University (YSU) PBL scheme. Both WRF datasets prescribe the heat and momentum fluxes to HYS-PLIT. These meteorological data are chosen for this study as they are the only non-hydrostatic meteorological data readily available.

Figure 7 shows the geopotential heights of the 925-hPa level, which represents the flow within the PBL, and thus, provides an approximation of the transport flow of the CAPTEX plumes. The charts are created with the NOAA Earth System Research Laboratory (ESRL) web plotter utilizing the NARR dataset. CAPTEX 1 featured a southwesterly gradient with 925-hPa winds between 20 and 30 knots (kts) through the sampling network before becoming more diffluent over New England as depicted in Figure 7a. The CAPTEX 2 release was conducted under the lightest wind conditions of all the releases, 5 to 10 kts, due to the presence of a high pressure center over the East Coast, as shown in Figure 7b. This means CAPTEX 2 was released in a meteorological environment with less synoptic, or large-scale, forcing than CAPTEX 1 as the weaker winds suppressed plume transport and allowed the random dispersive motions within the atmosphere to increase the spatial footprint

of the plume in all directions. Figure 7c shows ridging over the sampling network during the CAPTEX 3 release resulting in 925-hPa winds between 5 to 10 kts under the ridge axis with winds increasing to 20 kts in northern New York and southern Canada. This, like CAPTEX 2, provided a less synoptically forced environment for the plume transport. CAPTEX 4 shown in Figure 7d featured a west-southwesterly gradient supporting winds between 25 and 30 kts. In this case, the greater synoptic forcing confined the plume to a narrower footprint and transported it quickly through the sampling network similar to CAPTEX 1. As previously mentioned, both Sudbury releases occurred behind cold fronts to advect the tracer of PMCH into the sampling network to the southeast. Figures 7e and 7f depict the northwesterly gradient behind the cold fronts for CAPTEX 5 and 7, respectively. The 925-hPa winds for CAPTEX 5 were between 20 and 25 kts over the sampling network while CAPTEX 7 featured a stronger gradient supporting winds up to 35 kts. Thus, CAPTEX 2 and 3 provided the least synoptically-forced meteorological environment for the tracer plume, and the other releases featured stronger synoptic flow that inhibited the omnidirectional spatial expansion of their respective plumes as they were transported through the sampling network.

Stabilized Nuclear Clouds

In order to understand how to simulate nuclear fallout from a nuclear detonation within HYSPLIT, a stabilized nuclear cloud is defined. Rolph et al. (2014) utilized the concept of a stabilized nuclear cloud to simulate how the effects of an improvised nuclear device might be transported through the atmosphere. This study worked with data from the nuclear tests at the Nevada Test Site (NTS) from 1951 to 1957. Rather than explicitly simulating the nuclear detonation (NUDET) and subsequent introduction of radioactive particles into the atmosphere, a cloud containing the ra-
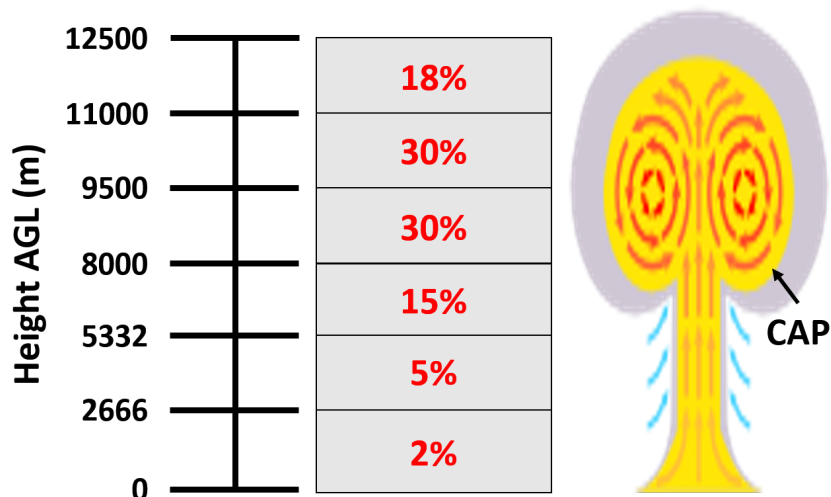
Figure 8. Activity distribution (in percentage) by height of a stabilized nuclear cloud originating from detonations with yields between 42.5 and 45 kT, such as both the Simon and Smoky NUDETs. Adapted from Rolph et al. (2014).

dioactive particles is created and initialized into HYSPLIT after the atmosphere has stabilized from the initial explosive effects.

First, the vertical extent of the cloud is directly proportional to the yield of the weapon employed. Additionally, the particle activity within the cloud is not uniform with height, but rather most of the activity is confined to the cap or top of the cloud. The cloud is divided into six layers and the activity level is defined by the work done within each level (Rolph et al. 2014). Similar to the vertical extent, the heights of each level are proportional to the yield of the weapon. Figure 8 depicts the activity level by height above ground level (AGL) for yields between 42.5 kiloton (kT) and 45 kT. Rolph et al. (2014) specified these release heights in HYSPLIT, which causes the model to release the particles along a vertical line within the cloud instead of across the diameter of the cloud. This is a reasonable assumption since the scale and resolution of the meteorological data and transport scenario are much greater than the width of the cloud.

Next, the particle sizes within the cloud are not uniform, but rather follow a

Particle Diameter (μm)	20	45	57.5	70	87.5	112.5	137.5	162.5	187.5	225	275	350	500
Activity Level (%)	12	8	10	10	18	12	8	6	4	5	3	3	1

Table 2. Activity level by percentage per particle diameter bin for the Glasstone Distribution.

prescribed percentage distribution based on particle diameter. While many different particle size distributions have been studied, this study focuses on the Glasstone Distribution. The diameter bins are obtain from Rolph et al. (2014), which is based on work by Glasstone and Dolan (1977). The activity percentage per particle size bin for this distribution is given in Table 2. Rolph et al. (2014) assumed these particles are soil particles with the radionuclides attached, and that they are spherical with a density of 2.5 g/cm^3. This affects the gravitational settling velocity of the dry removal of the particles, which contributes to the dose obtain from radionuclides deposited into the ground. While wet deposition is certainly possible, Rolph et al. (2014) neglected this as the nuclear detonation tests were conducted in the Nevada deserts at specific times to avoid rain events. These particles only encompass 17% of the total mass of the cloud as the other 83% consists of noble gases (Rolph et al. 2014). Thus, the particle activity levels were scaled by this factor when determining how much mass each particle size bin accounts for at each level within the cloud.

These assumptions in Rolph et al. (2014) that describe stabilized nuclear clouds create a dispersible feature within HYSPLIT, while avoiding the complexities of simulating an actual nuclear detonation. This allows HYSPLIT to transport and disperse the cloud through the prescribed meteorological fields and calculate air concentrations and deposition. The specifics of how this study configures HYSPLIT for stabilized nuclear cloud ensembles and how their dispersion is converted into a radioactive dose rate along the path of the advection of the clouds is discussed in the next chapter.

(a) 300-hPa

(b) 500-hPa
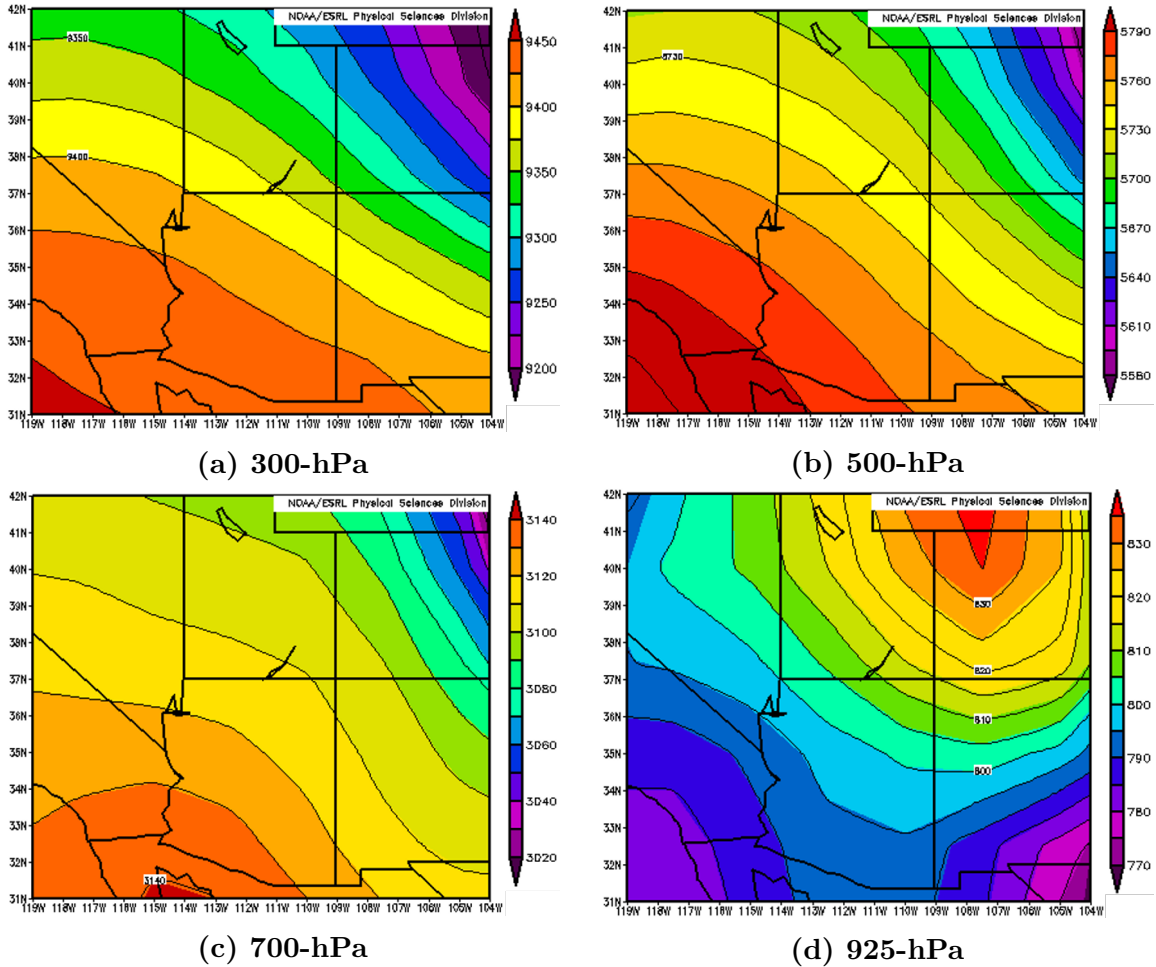
(c) 700-hPa

(d) 925-hPa

Figure 9. Geopotential heights in meters from the NCAR/NCEP Reanalysis dataset at the (a) 300-hPa, (b) 500-hPa, (c) 700-hPa, and (d) 925-hPa levels of the atmosphere at the time of the Simon detonation (25 April 1953 at 1200 UTC).

Nevada Test Site NUDETs Meteorological Data and Conditions

Three ARL-formatted meteorological datasets are available for the NUDETs that were tested at the NTS between 1951 and 1957. The first dataset is the National Centers for Environmental Prediction (NCEP)/National Center for Atmospheric Research (NCAR) Reanalysis, which has a resolution of 2.5° spanning the entire globe. This is much coarser than any of the meteorological data available for the CAPTEX simulations. The second and third datasets are 36-km and 12-km resolutions of the version 3.4.1 WRF model from Rolph et al. (2014), which utilized the YSU PBL

scheme. Ultimately, the highest resolution, the WRF 12-km dataset, is chosen for this study for reasons derived from the CAPTEX results. This reasoning is explained in Chapter IV.

With the near-surface CAPTEX releases, the main focus for the meteorological conditions is on the flow within the PBL as most of the plume remains in the PBL throughout its transport. However, stabilized nuclear clouds have much greater vertical extent, and meteorological conditions across the depth of the troposphere must be considered. Figure 9 depicts the geopotential heights for the 300-hPa, 500-hPa, 700-hPa, and 925-hPa levels, which correspond to the atmospheric flow at the upper level, mid-level, lower level, and within PBL of the troposphere, respectively, at the time of the Simon detonation. The charts are created from the ESRL web plotter utilizing NCEP/NCAR Reanalysis data. Ridging aloft at the 300-hPa and 500-hPa levels over southern California and Nevada supported a high pressure center at the 925-hPa level over Wyoming. This allowed for light and dispersive winds at the surface becoming more west-northwesterly with height. As most of the activity in the stabilized nuclear cloud is located in the cap that is centered about the 300-hPa level, this flow dictates the majority of the transport of the cloud. In this case, the debris from the actual nuclear detonation was advected by winds of 30 to 35 kts resulting in a fallout pattern extending to the east-southeast across southern Nevada and into Arizona. Thus, the higher winds in the upper levels limited the dispersion and width of the debris plume.

Figure 10 depicts a much different meteorological situation for the Smoky detonation than previously discussed with the Simon detonation. As before, the 300-hPa, 500-hPa, 700-hPa, and 925-hPa geopotential height levels are presented in meters derived from the NCAR/NCEP Reanalysis dataset with the ESRL web plotter. At the time of the Smoky detonation, an upper level low was centered over northern Nevada
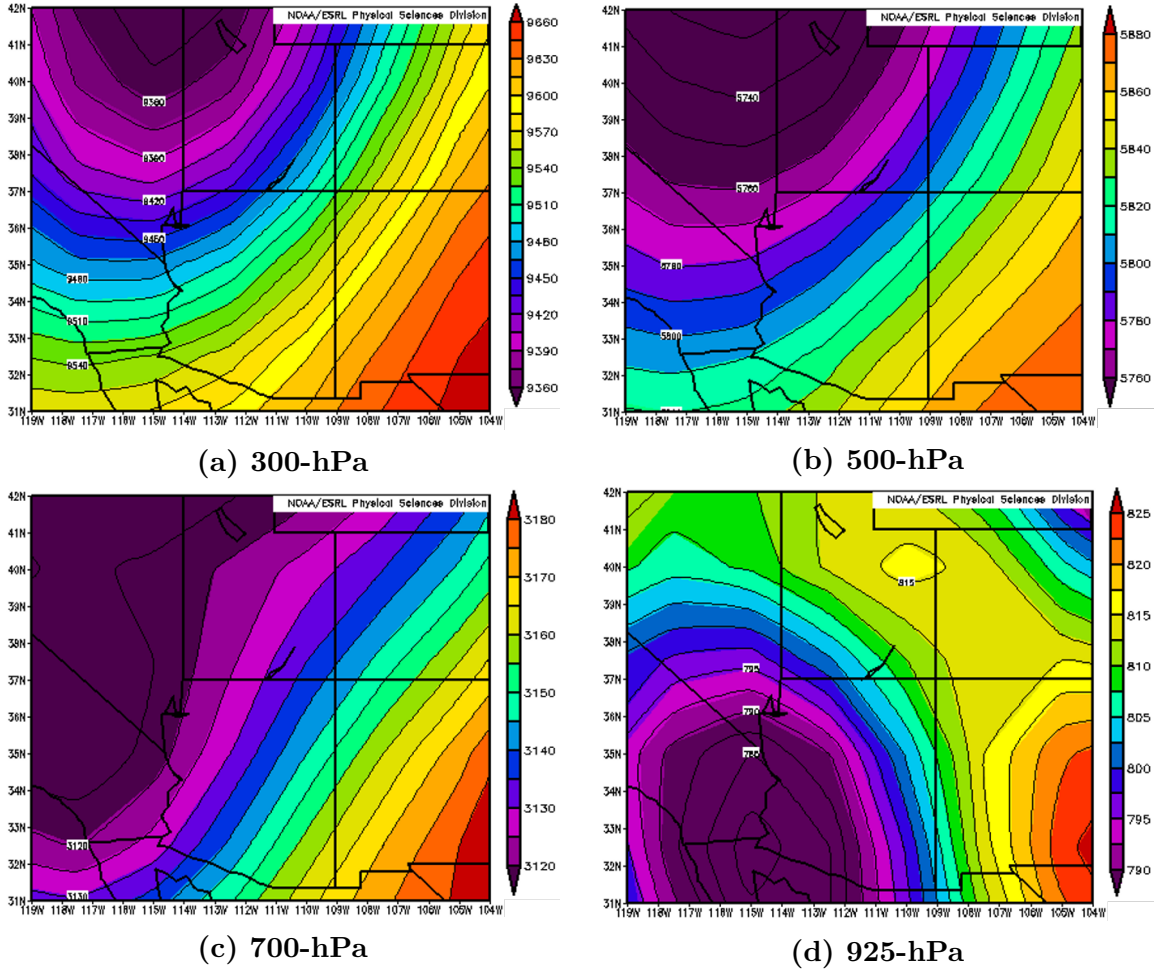
Figure 10. Geopotential heights in meters from the NCAR/NCEP Reanalysis dataset at the (a) 300-hPa, (b) 500-hPa, (c) 700-hPa, and (d) 925-hPa levels of the atmosphere at the time of the Smoky detonation (31 August 1957 at 1200 UTC).

and northern Utah that stacked down in the troposphere to support a 925-hPa low centered over the intersection of the borders of California, Arizona, and Mexico. The surface low pressure center was shallow at 1013 hPa compared to higher latitude low pressure systems, therefore, the winds within the boundary layer were light, specifically 5 to 10 kts out of the southeast over southern Nevada. These winds increased and veered, or rotated clockwise, with increasing height to 50 to 60 kts out of the west-southwest at the 300-hPa level. While these winds are still lighter than winds present in a 300-hPa jet core, they are still stronger than the winds present during

the Simon detonation resulting in more vertical wind shear presence throughout the troposphere at the time of the Smoky detonation. Thus, these two NUDET cases provide contrasting meteorological conditions on which to test the methodology of this study.

Summary

This chapter presented the two approaches to atmospheric transport and dispersion modeling and introduced the HYSPLIT model. Additionally, the experimental design of CAPTEX and meteorological conditions during the releases were characterized. Lastly, stabilized nuclear clouds were discussed along with the meteorological conditions that occurred at the time of the Simon and Smoky NUDETs. This provides two datasets on which the methodology of this study is tested. The next chapter describes this methodology and how it is configured in HYSPLIT.

III. Methodology

While the previous chapter described various approaches to STE and how HYS-PLIT simulates transport and dispersion within the atmosphere, this chapter discusses a specific methodology to estimate the source location of a plume of atmospheric pollutants. Specifically, this study uses a series of HYSPLIT forward concentration simulations to attempt to determine the correct source location. This can be thought as an ensemble of HYSPLIT runs with the starting location as the only varying parameter. The best performing ensemble member when compared to the actual observations is selected as the source location.

While backward simulations of trajectories within HYSPLIT are possible, HYS-PLIT is not capable of simulating a true backward dispersion. When the concentration model is run in reverse, the random turbulent motions added to the backward trajectories are still dispersing the plume in many directions. Thus, the backward plume becomes spatially larger even though it is propagating against the meteorological flow. Since the random motions of the dispersed particles cannot be reversed, concentration measurements cannot be backward-simulated and "un-dispersed." This is the primary reason why this study focuses on an ensemble of forward concentration simulations while storing the data in an SRM. This approach is first applied to data from the CAPTEX experiment followed by data from the NUDETs that occurred at the NTS from 1951 to 1957.

Source Grid and Source-Receptor Matrix

In order to find the actual release location of a pollutant plume using a series of forward concentration simulations, a grid of **possible** source locations—the source grid—is defined. This source grid spans the geographic area that may contain the
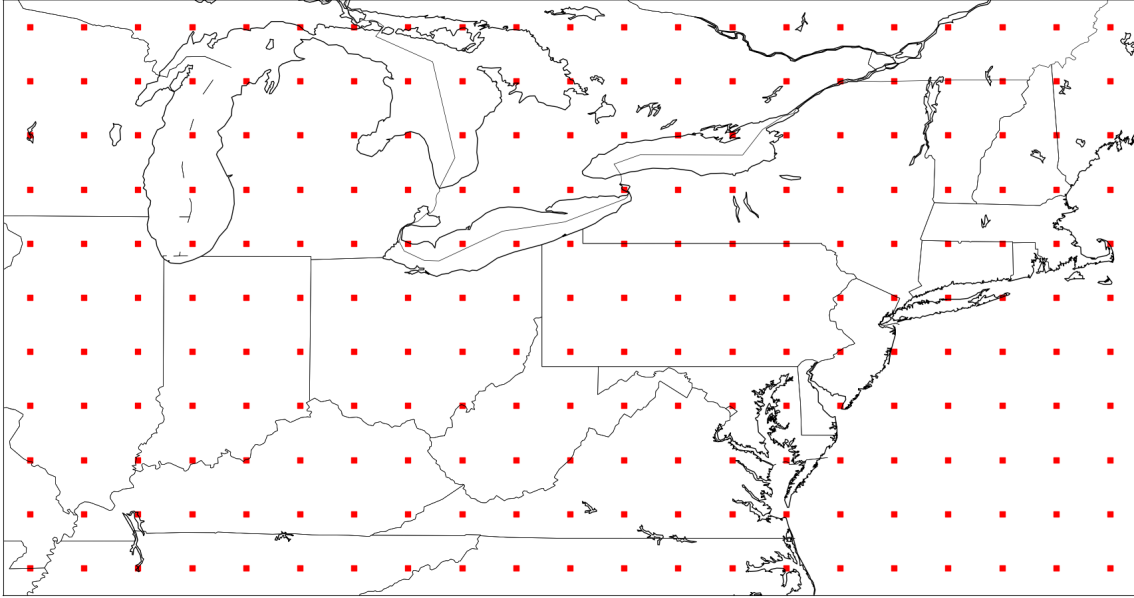
Figure 11. Example of a source grid used for the CAPTEX 1-4 releases. This grid is defined at 1° resolution where each red dot represents a possible source location that will be tested.

actual release site. Physical factors of meteorological conditions combined with the observed pollutant concentrations determine the initial iteration of the size and location of the source grid. Other factors such as computational and time resources can also dictate. Figure 11 shows the source grid defined for the CAPTEX 1-4 releases at 1° resolution.

If the parameters to assign the first iteration of the source grid are not obvious given the meteorological conditions and plume observations, a more expansive, coarser source grid can first be tested to help determine the domain and resolution of the subsequent source grid. The source grid resolution defines the precision of the STE solution: if a 2° resolution source grid is tested, the true source exists anywhere in between a 2° by 2° grid box. This level of precision is acceptable for determining a country or region from where a pollutant plume originates; corresponding finer resolution source grids are needed for potential increased STE accuracy. This finer resolution source grid costs greater computational expense. This study tests multiple
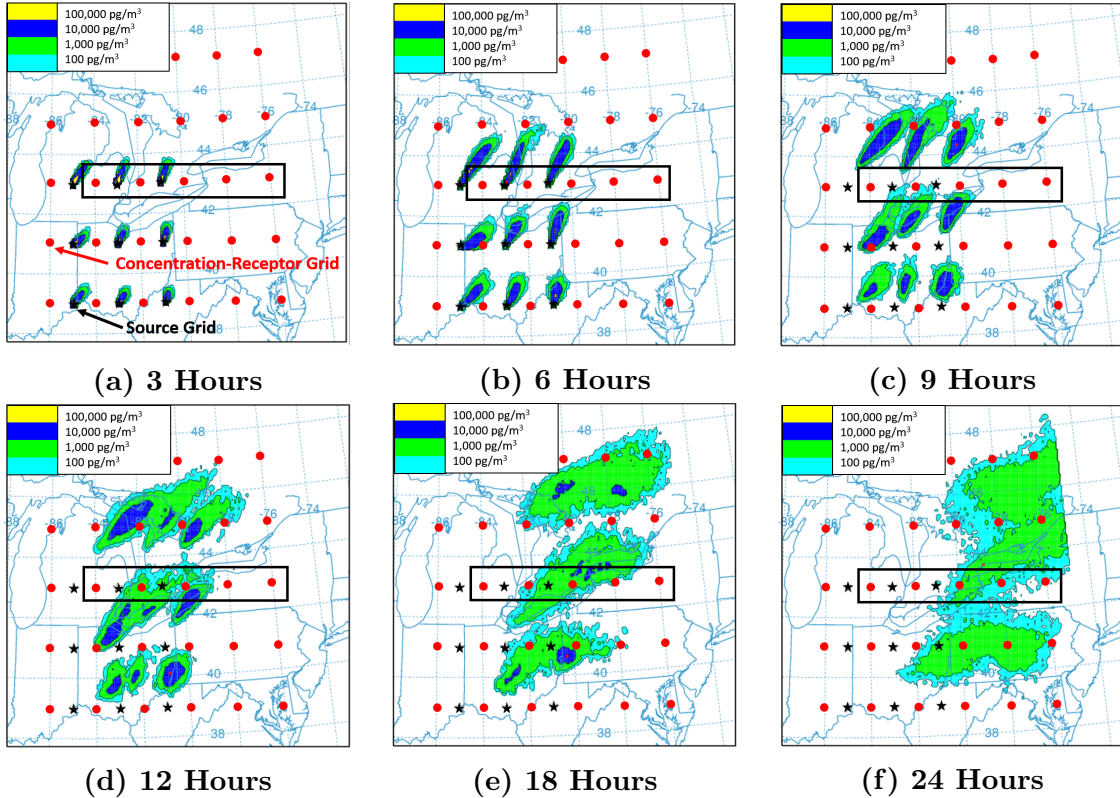
Figure 12. Time series of a 2° SRM at (a) 3 hours, (b) 6 hours, (c) 9 hours, (d) 12 hours, (e) 18 hours, and (f) 24 hours after the PMCH releases from each point on the source grid (black stars) as the plumes transit the concentration-receptor grid (red circles). HYSPLIT tracks the source location of each particle in order to extract the specific concentrations from each plume in later steps despite the plumes merging visually. The black box encloses the concentration-receptor grid points whose concentration values are featured in Table 3.

source grid resolutions over the same area using the same meteorological and observational data to determine under which combination of meteorological conditions and model data this greater computational expense provides a more accurate STE solution.

Standard output concentration files in HYSPLIT store the model-calculated concentrations of all particles at each point in the concentration-receptor grid for a specified time period. When an SRM containing multiple sources is configured within HYSPLIT, the concentrations are calculated from each source separately and stored in a column of a matrix. This is accomplished because HYSPLIT tracks from which

30

3 Hours	Source 1	Source 2	Source 3	Source 4	Source 5	Source 6	Source 7	Source 8	Source 9
Receptor 1	0	0	5000	0	0	0	0	0	0
Receptor 2	0	0	0	0	0	4800	0	0	0
Receptor 3	0	0	0	0	0	0	0	0	3200
Receptor 4	0	0	0	0	0	0	0	0	0
Receptor 5	0	0	0	0	0	0	0	0	0
6 Hours	Source 1	Source 2	Source 3	Source 4	Source 5	Source 6	Source 7	Source 8	Source 9
Receptor 1	0	0	4900	0	0	0	0	0	0
Receptor 2	0	1	100	0	13	4300	0	0	0
Receptor 3	0	0	0	0	1	0	0	220	3000
Receptor 4	0	0	0	0	0	0	0	0	6
Receptor 5	0	0	0	0	0	0	0	0	0
9 Hours	Source 1	Source 2	Source 3	Source 4	Source 5	Source 6	Source 7	Source 8	Source 9
Receptor 1	0	0	310	0	0	0	0	0	0
Receptor 2	0	400	18	0	270	490	0	0	0
Receptor 3	0	0	0	0	550	4	0	2100	230
Receptor 4	0	0	0	0	0	0	0	330	2
Receptor 5	0	0	0	0	0	0	0	0	0
12 Hours	Source 1	Source 2	Source 3	Source 4	Source 5	Source 6	Source 7	Source 8	Source 9
Receptor 1	0	0	0	0	0	0	0	0	0
Receptor 2	0	1500	0	0	19	0	0	0	0
Receptor 3	0	200	0	0	1100	0	0	680	0
Receptor 4	0	4	0	0	150	0	0	2200	0
Receptor 5	0	0	0	0	0	0	0	1	0
18 Hours	Source 1	Source 2	Source 3	Source 4	Source 5	Source 6	Source 7	Source 8	Source 9
Receptor 1	0	0	0	0	0	0	0	0	0
Receptor 2	0	63	0	0	0	0	0	0	0
Receptor 3	1	2100	0	2	87	0	0	0	0
Receptor 4	0	650	0	2	1200	0	0	1400	0
Receptor 5	0	0	0	0	61	0	0	780	0
24 Hours	Source 1	Source 2	Source 3	Source 4	Source 5	Source 6	Source 7	Source 8	Source 9
Receptor 1	0	0	0	0	0	0	0	0	0
Receptor 2	0	0	0	0	0	0	0	0	0
Receptor 3	1	140	0	2	0	0	0	0	0
Receptor 4	7	1500	0	22	160	0	0	47	0
Receptor 5	1	290	0	7	270	0	1	450	0

Table 3. Time series of PMCH concentrations calculated in picograms from each source as measured by the five boxed receptors in Figure 12. Receptors are numbered from west to east.

source each particle originates. Figure 12 depicts an example of a time series of a 2° SRM simulation over a subset of the CAPTEX domain. While this figure shows a visually merged field with contributions from multiple sources arriving at an individual concentration-receptor, the sources are fully separable, allowing interrogation of source origin. Thus, the time evolution of the concentrations from each source can be extracted. Table 3 shows the concentration extractions of all nine sources in Figure 12 as the plumes are transported through five selected receptors. In this way, the arrival and departure of the plumes from each source is seen in the row of each receptor. Additionally, the eastward progression of the plumes originating

from each source is evident in the columns of the table. With an SRM, an ensemble of concentration simulations with varying source locations is conducted in a single HYSPLIT run. For this study, the source grid and concentration-receptor grid are set to the same resolution, though the points on the source grid are not necessarily co-located with the points on the concentration-receptor grid as the two grids operate independently within HYSPLIT. Therefore, the resolution of the SRM refers to both the resolution of the source grid and concentration-receptor grid.

Model Rank

HYSPLIT uses the model rank as a metric to compare the accuracy of each modeled concentration plume within the SRM to the actual observed plume. This is accomplished by combining several statistical parameters to define the holistic model rank metric where the highest scoring modeled concentration plume is assumed to be the closest to the observed plume from the actual release location. First, the linear correlation coefficient (R) measures the scatter in the data field between the paired measured and predicted values:

$$R = \frac{\sum_i (M_i - \bar{M})(P_i - \bar{P})}{\sqrt{\sum_i (M_i - \bar{M})^2 (P_i - \bar{P})^2}}, \tag{17}$$

where $\bar{M}$ and $\bar{P}$ are the means of the measured and predicted values, respectively, and M_i and P_i are the i-th measured and predicted pair values, respectively (Draxler 2006). Second, the fractional bias (FB) is the normalized measure of the bias, which is the average difference between the prediction-measurement pairs:

$$BIAS = \frac{1}{N} \sum_i (P_i - M_i) \rightarrow FB = \frac{2\bar{B}}{\bar{P} + \bar{M}}, \tag{18}$$

where N is the number of prediction-measurement pairs (Draxler et al. 2001). Thirdly, the figure of merit in space (FMS) evaluates the spatial distribution of HYSPLIT-predicted values against the spatial distribution of measurements regardless of absolute concentration amount:

$$FMS = 100 * \frac{N(P_i > 0) \cap N(M_i > 0)}{N(P_i > 0) \cup N(M_i > 0)}, \tag{19}$$

which is the intersection of the predicted and measured values above zero concentration units divided by the union of the predicted and measured values above zero concentration units for each time step (Draxler et al. 2001). The only unpaired statistic used is the Kolomogorov-Smirnov (KS) parameter that measures whether HYSPLIT reproduces the measured concentration distribution regardless of when or where the values were predicted (Draxler 2006). It is defined as the maximum difference between the cumulative distribution functions (CDFs) of the measured and predicted values (Draxler 2006):

$$KS = 100 * \max \mid CDF(M) - CDF(P) \mid . \tag{20}$$

Finally, the statistics are combined to define the final model ranking in order to make comparisons:

$$RANK \equiv R^2 + \left(1 - \mid \frac{FB}{2} \mid\right) + \frac{FMS}{100} + \left(1 - \frac{KS}{100}\right), \tag{21}$$

where the best model ranking would be 4.0 (Draxler et al. 2001). Thus, the model rank scores the plume associated with each source location based on its temporal, spatial, and overall distribution accuracy.

CAPTEX Simulations

This study first utilizes data from CAPTEX releases 1-5 and 7 to test the SRM approach to STE. Because the CAPTEX 6 release was shorter in duration with smaller plume extent, the data associated with this release is excluded for comparison purposes. In comparing CAPTEX releases 1-5 and 7 releases, which occurred during varied meteorological conditions, sensitivities of the SRM method can be discovered.

First, HYSPLIT is configured to run one SRM for each resolution for each release. This study assumes the time of the pollutant release is known through other methods, thus, HYSPLIT is set to begin each release according to the times and durations listed in Table 1. Additionally, the amount of mass released at each grid point on the source grid is the same as was released for that particular CAPTEX release. Checking the output MESSAGE file, which shows the total mass in the simulation for each time step, verifies this. For example, the CAPTEX 1 source grid with 0.5° resolution contains 861 grid points with each releasing 208 kg of PMCH. Consequently, the MESSAGE file shows 208 kg for each of the 861 grid points, resulting in 179,088 kg of PMCH in the simulation during the time steps immediately following the completion of the release. HYSPLIT releases the PMCH at 10 m AGL at each source grid point.

	Number of Sources Tested	
Source Grid Resolution	CAPTEX 1-4	CAPTEX 5 & 7
2°	66	88
1°	231	315
0.5°	861	1189
0.25°	3321	4617
0.1°	20301	Not Tested

Table 4. Number of possible sources tested for each resolution for the two CAPTEX source grids.

Source Grid Resolutions

Although only CAPTEX plumes were only released from two geographic locations, Dayton and Sudbury, multiple source grid resolutions are tested. For CAPTEX 1-4, the source grid covers the area bound by 36-46°N and 70-90°W. The grid for CAPTEX 5 and 7 contains the same geographic area but extends north to 50°N. This extension is necessary because Sudbury, ON, lies on the boundary of the CAPTEX 1-4 source grid. While it is not reasonable to expect the actual release location be centered in the user-selected source grid, in order to mitigate boundary effects, this study adjusts the source grid for CAPTEX 5 and 7 to the north. Within these source grids, resolutions of 2°, 1°, 0.5°, and 0.25° are tested.

Additionally, for CAPTEX 1-4, a 0.1° source grid is also tested, as the computational expense limited its implementation on CAPTEX 5 and 7. Table 4 shows the number of sources tested for each source grid resolution. In order to define these source grids in HYSPLIT, three points are input to the CONTROL file: the southwest-most (lower-left) point, the northeast-most (upper-right) point, and the next closest grid point northeast of the first point. The first two points set the domain of the source grid, the third sets the resolution. For example, the points (36°N, 90°W), (46°N, 70°W), and (37°N, 89°W) define the 1° resolution source grid for the CAPTEX 1-4 simulations. A preprocessing program rewrites the CONTROL file to contain the latitude and longitude of all the possible sources located within the source grid.

Concentration-Receptor Grid Resolutions

Next, concentration-receptor grids are defined to complete the CAPTEX SRM configuration. All CAPTEX releases utilize the same geographic area for the concentration grid. In HYSPLIT, the concentration-receptor grid is centered on the point (42°N, 78°W), which is central to the observing stations, and extends 7.5° latitudi-

nally and 12.5° longitudinally in both directions. The concentration-receptor grid extends vertically from the ground to 100 m AGL to adequately sample the concentrations present within the HYSPLIT-modeled PBL. No deposition is configured for these simulations, thus, a ground-level deposition grid is not required. As with the source grid, multiple resolutions are tested within the concentration-receptor grid to test the sensitivity of the STE solution to this parameter. 2°, 1°, 0.5°, 0.25°, and 0.1° resolutions are tested, which spans the range of distances the CAPTEX observing stations are apart from each other. While the CONTROL file can be configured for any combination of source grid-concentration-receptor grid resolutions, this study matches the source grid resolution to the concentration-receptor grid resolution. For the remainder of this paper, these two resolutions will simply be referred to as the resolution of the SRM unless otherwise specified.

Sampling start, stop, and frequency are also defined in the concentration-receptor grid. All CAPTEX releases are configured with 3-hour sampling averages as actual CAPTEX observations are given as either 3-hour or 6-hour averages. With a binary file of 3-hour averages, the Data Archive of Tracer Experiments and Meteorology (DATEM) extraction program is able to create 6-hour averages by combining two 3-hour averages. The concentration-receptor grid begins sampling at the same time as the first observation in the observation file of each release. It continues sampling until a few hours after the last observation is made to ensure the DATEM extraction program has enough time periods within the concentration-receptor grid. This varies based on release. The overall HYSPLIT simulation begins at the release time and continues beyond the concentration sampling period. Table 5 lists the specific times for the beginning and termination of the concentration-receptor grid sampling for each CAPTEX release along with the overall duration of the HYSPLIT simulation.

Release	Concentration Grid Start (UTC)	Concentration Grid Stop (UTC)	Overall Simulation Duration (Hours)
CAPTEX 1	18 Sep 1983 1800	21 Sep 1983 1500	70
CAPTEX 2	25 Sep 1983 1800	28 Sep 1983 1500	68
CAPTEX 3	02 Oct 1983 2100	05 Oct 1983 2100	74
CAPTEX 4	14 Oct 1983 1800	17 Oct 1983 0300	59
CAPTEX 5	26 Oct 1983 0900	28 Oct 1983 1200	56
CAPTEX 7	29 Oct 1983 0600	31 Oct 1983 1500	57

Table 5. Model concentration-receptor grid sampling start and stop times and overall simulation duration for each CAPTEX release. The overall duration exceeds the concentration-receptor sampling duration to ensure dispersion calculations continue beyond the sampling period.

Particles and Chemistry

The final step before running HYSPLIT is configuring the namelist. Only three parameters are changed from the defaults for this study. First, the number of particles released at each source is set to 50,000 per cycle with the maximum number of particles set to 100,000. This provides enough particles to adequately represent the dispersion of the pollutant plume without causing extra computational overhead. Finally, the in-line chemical conversion module (ICHEM) namelist variable is changed to "1," which reconfigures the standard concentration-receptor grid to the SRM. This tells HYSPLIT to track the particles from each source independently and store their concentrations in the SRM. Of note, since no turbulence method is passed in the namelist for this study, the default turbulence parameterization, Kantha-Clayson, is selected during the HYSPLIT run.

With the model properly configured for an SRM simulation of each CAPTEX release, HYSPLIT is run. HYSPLIT calculates dispersion from each point and stores

Meteorological Data Available						
CAPTEX Release	1	2	3	4	5	7
NARR 32.5-km	X	X	X	X	X	X
27-km WRF (Ngan and Stein 2017)	X	X	X	X	X	X
9-km WRF (Ngan and Stein 2017)	X	X	X	X	X	X
3-km WRF (Tutorial) Nested in 9-km WRF (Ngan and Stein 2017)		X				
27-km WRF (Tutorial)		X				
9-km WRF (Tutorial)		X				
3-km WRF (Tutorial) Nested in 9-km WRF (Tutorial)		X				
SRM Resolutions Tested						
2°	X	X	X	X	X	X
1°	X	X	X	X	X	X
0.5°	X	X	X	X	X	X
0.25°	X	X	X	X	X	X
0.1°	X	X	X	X		

Table 6. Summary of the availability of the meteorological datasets for each CAPTEX release. The corresponding SRM resolutions are tested for each of the meteorological datasets available.

the resulting concentrations from each source in the SRM that is specified in the CON-TROL file. This results in an output binary file containing the SRM. This process is repeated for each release with varying SRM resolutions and meteorological input files. Each release is tested with NARR meteorological data and 27-km and 9-km WRF meteorological data from Ngan and Stein (2017) utilizing the MYNN PBL scheme. Additionally, 27-km, 9-km, and 3-km WRF data from the HYSPLIT Tutorial, which utilizes the YSU PBL scheme, are available for CAPTEX 2. This allows for comparisons between how the different parameterizations in the meteorological model affect the STE solution. For each meteorological data file per release, SRM resolutions of

2°, 1°, 0.5°, 0.25°, and 0.1° are tested. Therefore, one HYSPLIT run consists of a CAPTEX release simulated with a particular meteorological dataset, at a particular SRM resolution. Table 6 summarizes the meteorological datasets available for each CAPTEX release along with the SRM resolutions to be tested.

Post-processing

In order to determine the best performing sources within the SRM output binary file, several post-processing programs are utilized. The first program, **MATRIX**, extracts the specific concentration binary data from one source within the SRM. The program pulls one column of HYSPLIT concentration calculations belonging to one source from the SRM. This isolates a particular model pollutant plume to score its performance against the actual CAPTEX observations. The next program, **C2DATEM**, converts the individual binary file of this source into the DATEM text file format by matching observation times and locations given in the observational CAPTEX DATEM text file. Since the observation locations do not necessarily coincide with a model concentration-receptor grid point, the nearest grid points are bilinearly interpolated to the observation location. Additionally, the concentration values are multiplied by 10^{12} to match the units of the observation file in picograms. A statistics program, **STATMAIN**, then compares the model-derived DATEM file to the CAPTEX observed DATEM file and calculates R, FB, FMS, the KS parameter, and the final model rank derived using the equations previously discussed. The results for each source are appended to a summary text file. These programs are available within the standard HYSPLIT distribution as compiled Formula Translation (FORTRAN) executable files.

The final step to determining the possible source location of the PMCH release is to find the highest scoring source location within the summary text file based on

model rank. A Python program reads the file and identifies the highest ranking source location. However, this is not necessarily the final STE solution. Any sources scoring within 0.1 model rank of the highest scoring source are not performing statistically significantly worse than the highest source, therefore, these must also be included in the STE solution (Air Resources Laboratory 2018b). Thus, the highest scoring source is determined within the file and 0.1 is subtracted from its model rank to create a threshold model rank. Any source scoring equal to or higher than this threshold is considered a possible source location based on the HYSPLIT simulation and observational data supplied. The program also computes distances from the actual CAPTEX release location for each of the identified source locations and calculates the mean distance error of all the possible sources. Thus, the final STE solution contains a range of possible source locations that cannot be statistically discriminated against one another as the best answer. It is possible for a solution to contain only one source location where no other sources scored within 0.1 model rank.

Sensitivities of the STE solution are tested by repeating the source scoring process described above while changing the observational data supplied to **C2DATEM**. By removing observations from the measurement file, HYSPLIT is scored against the remaining observations. This determines how specific observations change the STE solution. Since the same SRM data is ingested in the post-processing step leading into the DATEM conversion, there is no need to rerun the HYSPLIT SRM simulation to conduct these sensitivity analyses.

Two types of observation exclusion experiments, temporal sensitivity and spatial sensitivity, are conducted on the HYSPLIT SRM output for each meteorological model and SRM resolution listed in Table 6. First, this study removes observations on the basis of their sampling time. The sources are scored against an observation file containing all the observations except those taken within the first six hours. By

comparing this STE solution to the previous solution consisting of all the observations, the relative importance of those observations sampled within the first six hours is apparent. This process is repeated by excluding observations within the first 12, 18, 24, 36, and 48 hours for CAPTEX 1-4 and within the first 12, 18, 24, and 36 hours for CAPTEX 5 and 7, since those releases had shorter sampling durations. This process simulates deployment of samplers after a pollutant release to determine how quickly sampling must begin in order to reliably obtain a STE solution with the SRM methodology.

The second exclusion criteria this study utilizes is distance from the actual CAPTEX release location. The stations are grouped into 100-km radii: stations located less than or equal to 300 km, between 300-400 km, 400-500 km, 500-600 km, 600-700 km, 800-900 km, 900-1000 km, 1000-1100 km, and beyond 1100 km from the CAPTEX release location. The sources within the SRM are scored multiple times: each time excluding a different radius of station observations taken throughout the CAPTEX release regardless of the time they were sampled. This determines which radii away from the actual release location are most important to sample in order to calculate an accurate STE solution. Also, the average elevation of the radius excluded is calculated to determine how terrain affects the STE solution. This aids in developing sampling strategies for future real-world releases of contaminants into the atmosphere.

Nevada Test Site NUDETs Simulations

This study aims to test the SRM approach in a more complex, smaller scale simulation with non-inert pollutants. Nuclear tests conducted between 1951 and 1957 at the NTS fit these criteria. The SRM methodology is applied from the CAPTEX data to these NUDETs while incorporating HYSPLIT techniques from Rolph et al.

41

(2014) in order to model the fallout from stabilized nuclear clouds. Specifically, this study applies this methodology to the Simon and Smoky NUDETs, as these were the best and worst performing HYSPLIT simulations according to Rolph et al. (2014), respectively, determined by the FMS. Due to the complexity of these tests, modifications are made to the SRM approach in order to increase its ability to determine a reliable STE solution.

Running all the plumes on the defined source grid simultaneous releases the pollutants on one level. Also, only one concentration grid can be specified. For these reasons, running the SRM within a single HYSPLIT run is not possible, and instead, each source on the source grid requires its own distinct HYSPLIT simulation. This greatly increases computational expense, but allows for increased flexibility and complexity within each simulation. Preprocessing scripts ingest a list of the latitudes and longitudes of each location on the source grid and build the files required to run HYSPLIT specific to the simulation of each source. Each source is given a number that is appended to its preprocessing files. Therefore, HYSPLIT ingests the specific configuration files of that source. These simulations are conducted at a Department of Defense (DoD) high performance computing (HPC) center to decrease processing times.

The same assumptions regarding the time of the release and the type of emission are made just as with the CAPTEX releases. The CONTROL files are configured for the detonation times of both shots. Simon was detonated at 1200 Coordinated Universal Time (UTC) on April 25, 1953, and Smoky was detonated at 1200 UTC on August 31, 1957 (Rolph et al. 2014). Seven release levels are programmed into the CONTROL file whose heights are determined by the yield of each weapon, which was 43 kT for Simon and 44 kT for Smoky. Table 7 reflects the heights of each level for each weapon test. The top of HYSPLIT is also increased to 20,000 m to accommodate

the height of the nuclear clouds being modeled. The model is configured to release 13 particle sized and one noble gas. The release duration is set to one minute to simulate the quick introduction of nuclear fallout into the atmosphere as would occur during a nuclear bomb detonation. It is important to note the HYSPLIT is not explicitly simulating the explosive effects of the weapon or the detonation itself. The model is merely creating the fallout cloud in the first minute of the simulation, then modeling its transport and dispersion thereafter. To capture this, two concentration grids are necessary. One grid is set at ground level to measure the deposition of the fallout and the second extends from the ground to 100 m to measure air concentrations. Both are required to compute the total dose from air and ground exposure to radionuclides.

Rather than simulating radioactive decay directly in HYSPLIT, which is computationally expensive, dilution factors are calculated downwind from the detonation. Releasing one unit of mass during the detonation results in the deposition and concentration grids functioning as dilution factors that can be scaled by the yield of the weapon to calculate the dose rate. Therefore, the particle distribution throughout the cloud must be scaled in accordance with the Glasstone particle distribution adjusting for the fact that 83% of the activity is noble gases as well as the nuclear activity percentage by height previously discussed (Rolph et al. 2014). The specific mass released for each particle size at each level is shown in Table 7 and ingested into HYSPLIT from a separate emissions file. As HYSPLIT emission rates are expressed in units per hour, 60 units are specified in the emissions file so that one unit is emitted during the prescribed one-minute emission. Because one unit of mass is being released, which allows the downwind concentration values to function as dilution factors, the actual units of mass are arbitrary at this step. This study assumes that each particle has a density of 2.5 g/cm^3 and a spherical shape. Deposition velocities are diagnosed based on these attributes as no other explicit deposition velocities are prescribed.

Height (m)	Particle Diameter (μm)														Total
	GAS	20	45	57	70	87.5	112.5	137.5	162.5	187.5	225	275	350	500	
0	1.245	0.0306	0.0204	0.0306	0.0204	0.04335	0.0306	0.02295	0.0153	0.0102	0.01275	0.00765	0.0051	0.0051	1.5
2666	2.49	0.0612	0.0408	0.0612	0.0408	0.0867	0.0612	0.0459	0.0306	0.0204	0.0255	0.0153	0.0102	0.0102	3
5332	7.47	0.1836	0.1224	0.1836	0.1224	0.2601	0.1836	0.1377	0.0918	0.0612	0.0765	0.0459	0.0306	0.0306	9
8000	14.94	0.3672	0.2448	0.3672	0.2448	0.5202	0.3672	0.2754	0.1836	0.1224	0.153	0.0918	0.0612	0.0612	18
9500	14.94	0.3672	0.2448	0.3672	0.2448	0.5202	0.3672	0.2754	0.1836	0.1224	0.153	0.0918	0.0612	0.0612	18
11000	8.715	0.2142	0.1428	0.2142	0.1428	0.30345	0.2142	0.16065	0.1071	0.0714	0.08925	0.05355	0.0357	0.0357	10.5
12500	0	0	0	0	0	0	0	0	0	0	0	0	0	0	0
Total	49.8	1.224	0.816	1.224	0.816	1.734	1.224	0.918	0.612	0.408	0.51	0.306	0.204	0.204	60

Table 7. Units of mass released by particle size and by height within the stabilized nuclear cloud for the Simon and Smoky nuclear detonations. Units sum to 60 so one unit of mass is released during the one-minute emission (1/60th of an hour, as HYSPLIT computes mass emission rates in units per hour).

The namelist file consists of three main changes from the default configuration. First, the number of particles released per cycle and the maximum number of particles is set to 15,000 and 200,000 particles, respectively. Next, the ICHEM variable is set to "5," which causes mass to be removed from particles probabilistically as they interact with the deposition layer. The last namelist configuration allows for a more continuous size distribution of particles throughout the fallout cloud. As in Rolph et al. (2014), this study redistributes each particle size into five particle bins centered on the initially specified particle size. This increases the 14 particle bins to 70 bins allowing for a more comprehensive distribution of particle sizes throughout the stabilized nuclear cloud.

A script runs HYSPLIT with these configurations varying only the starting latitude and longitude according to the source locations specified in the source grid. This results in a series of output binary files containing the deposition and concentration dilution factors for each source simulation. These dilution factors are converted to dose rates through a series of post-processing steps before being compared to the Town Database, which contain the dose rates observed 24 hours following the actual bomb detonations. The first program, **CON2REM**, performs the initial concentration to dose rate conversion based on the dilution factors contained in the binary file and the yield of the weapon. The dose in Roentgen equivalent man (rem) at grid

space (i, j) from n radionuclides is calculated by:

$$DOSE_{i,j} = C_{i,j} \cdot Y \cdot T \cdot \sum_{s=1}^{n} [A_s \cdot D_s \cdot DCF_s], \tag{22}$$

where $C_{i,j}$ is the concentration in m^{-3} or deposition in m^{-2} dilution factor output by HYSPLIT, Y is the yield of the weapon in kT, T is the exposure time in hours, A_s is the radioactivity for nuclide s in Becquerel (Bq) per kT, D_s is the decay factor based on the half-life of nuclide s, and DCF_s is the dose conversion factor for nuclide s in rem·hr^{-1}·Bq^{-1}·m^3 (Rolph et al. 2014). The radioactivity, half-lives, and dose rate conversion factors for 213 radionuclides in a uranium-235 (U-235) weapon exist in a text file that is ingested by **CON2REM** for use in the dose rate calculation. By omitting the time exposure component, the program is set to calculate dose rates to match the Town Database. The program also decays all the doses backward in time to match the time of the observations file. This conversion accounts for the doses from air shine, ground shine, and inhalation by using both the air concentration and ground deposition dilution factors. and outputs the dose rates into a new binary file.

Even though the dilution factors are converted, these dose rates still exist on an air concentration grid and a ground deposition grid in the binary file. The next program, **CONCSUM**, sums the dose rates on both grids at every grid point creating another new binary file with the total dose rate for each grid point. This summed dose rate file is handled the same as the output concentration file in the CAPTEX simulations: **C2DATEM** extracts the model-derived dose rates at the points and times specified in the observational file, and **STATMAIN** calculates the same statistics as previously discussed by comparing the model-derived and observed dose rates at each reporting station. The top performing source locations determined by either FMS or model rank are considered to be possible locations of the actual bomb detonation.

This methodology is repeated using a higher resolution, smaller source grid defined
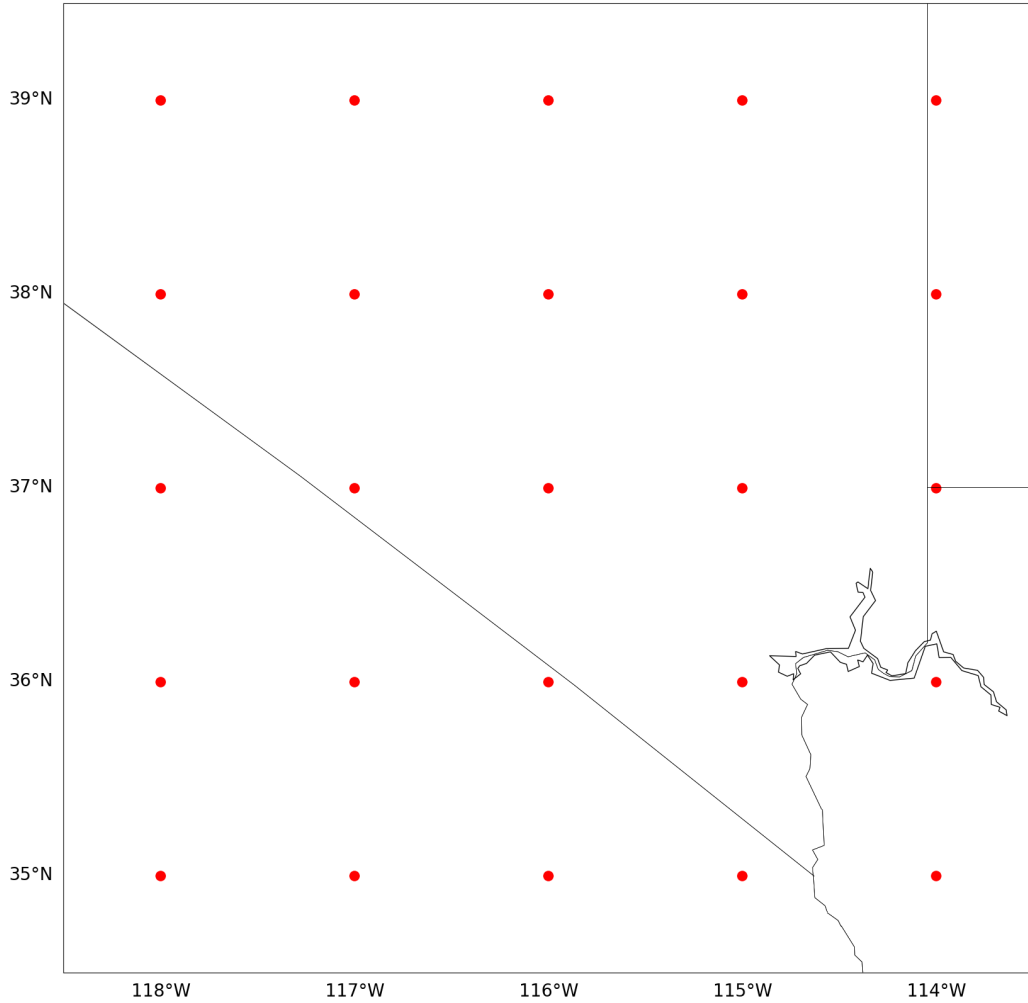
Figure 13. The locations (red points) of the first 25 sources tested for the Simon and Smoky NUDETs. Subsequent higher resolution source grids are tested based on the performance of these initial sources.

by the highest performing sources from the previously tested source grid. In this way, subsequent source grids can be tested at higher resolutions in order to obtain a more precise STE solution while minimizing computational expense. Thus, source areas that did not score well in the previous test will not be tested at higher resolutions. The resolution of the concentration and deposition grids are also increased as the source grid resolution is increased. Both of the Simon and Smoky NUDETs utilize an initial 1° resolution source grid spanning an area between 35-39°N and 114-118°W. Figure 13 displays the locations of these 25 sources spanning Nevada, California,

Arizona, and Utah. Concentration and deposition resolutions of 2°, 1°, 0.5°, 0.25°, and 0.1° are tested with the initial 1° source grid. Subsequent higher resolution source, concentration, and deposition grid resolutions are discussed in the following chapter, as these specifications depend on the results of the preceding test.

Summary

This chapter establishes the methodology utilized to estimate the source location of six CAPTEX releases and two nuclear bomb detonations by running an ensemble of HYSPLIT forward concentration simulations where the model release location is varied. For the CAPTEX simulations, the output is stored in an SRM. The model-derived concentrations from each source are extracted from the SRM and compared to the concentrations observed by the sampling stations to determine a model rank. The highest scoring sources are considered to be possible location of the true CAPTEX release location. By repeating the scoring while excluding observational data on the basis of time and distance from the release site, temporal and spatial sensitivities of the STE solution are determined.

Overall, the methodology and results from the CAPTEX simulations serve as a testbed to apply this STE technique to the more complex NUDET scenario. This process is applied to the Simon and Smoky nuclear tests. Due to the complexity of modeling stabilized nuclear clouds in HYSPLIT, each source requires an independent simulation whose output is stored in an independent binary file. Each binary file is converted to a dose rate and compared to observations from the Town Database. The highest scoring sources determine a new source grid that is tested at higher resolutions in order to achieve a more precise STE solution.

IV. Analysis and Results

The CAPTEX observational dataset serves as a testbed to study the effectiveness of the SRM methodology described in Chapter III. Specifically, due to the varied meteorological conditions that occurred during the CAPTEX releases as discussed in Chapter II, how these conditions affect the STE solution can be determined when they are ingested into HYSPLIT. The results from CAPTEX 1-4 are presented and discussed in this chapter; the CAPTEX 5 and 7 results are available in Appendix B. Additionally, this chapter discusses the results of the SRM methodology applied to the more complex nuclear tests at the NTS.

Results: CAPTEX 1983

For each of the CAPTEX releases (Table 6), a comparison of the model output to all observational data available yields a baseline STE solution. Following the initial STE solution, subsequent solutions are recalculated while excluding observations along the temporal axis. This simulates delaying the beginning of the observation record from the start of the actual pollutant release, as might occur in a real scenario where deployment of monitoring equipment may prevent sampling the plume in the hours immediately following its release. The reliability of the STE solution is judged as the included time period of observations becomes increasingly farther temporarily from the actual release time and presented in color-coded tables. The top performing

Color	STE Solution Criteria
	Within $\pm$ 1° of true source, no false solutions
	Within $\pm$ 2° of true source, and/or possible false solutions
	More than 2° from true source, and/or many false solutions

Table 8. Criteria applied to the STE solutions for the CAPTEX temporal exclusion tests. The degree separations are considered in both the latitudinal and longitudinal directions.
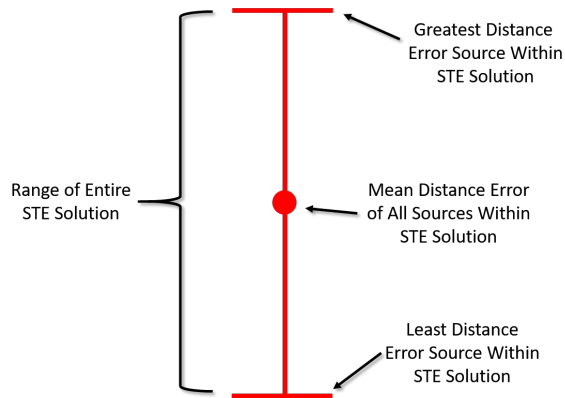
Figure 14. Explanation of plot elements for the distance sensitivity test results. The STE solution contains all sources scoring within 0.1 model rank of the highest scoring source. The upper and low horizontal bars represent the range of the distance errors within the STE solution. The dot is the mean distance error of all the sources within the STE solution. A dot without whiskers indicates the solution only contains one source (no other sources scored within 0.1 model rank of that source).

sources, within 0.1 model rank of the highest scoring source, are evaluated utilizing the criteria in Table 8 and are separated into three colors: green, yellow, and red. *Green* indicates the highest scoring sources are all within ± 1° latitudinally and longitudinally of the actual CAPTEX release location. *Yellow* specifies that the highest performing sources are within ± 2° latitudinally and longitudinally of the actual CAPTEX release location. *Yellow* also indicates the presence of a few false solutions: high scoring solutions that are not within the bounds meeting the green criteria. This means a reliable STE solution exists, but there are contaminating solutions not statistically significantly different from the reliable solution. *Red* specifies that none of the highest scoring sources are within ± 2° latitudinally and longitudinally of the actual CAPTEX release location, or that so many false solutions are present that it would be impossible to choose the best STE solution with any statistical basis.

As discussed in Chapter III, the HYSPLIT SRM output is also compared to the observational data while iteratively excluding station reports in specified radii away from the actual release location. As with the temporal sensitivity tests discussed in the previous paragraph, the highest scoring sources are considered the STE solution,

49

and the distance from each of the sources to the true source is averaged and shown in a line plot. The spread in the distances of the sources for each radius excluded is also plotted, in addition to the mean elevation of the excluded stations. Figure 14 summarizes the data representation of these line plots. Thus, the results of each CAPTEX release contain stoplight charts indicating the temporal sensitivity and line plots displaying the observational distance sensitivity of the STE solution.

CAPTEX 1

The first CAPTEX release occurred on September 18, 1983 at 1700 UTC with observations measured as late as 61 hours following the beginning of the emission. The meteorological conditions included a well-defined geopotential height gradient below the 850-hPa level that transported the actual plume northeastward from Dayton to Lake Eerie before turning eastward over Pennsylvania. Table 9 summarizes the results of the first temporal sensitivity tests for the horizontal resolution-varying meteorological datasets. The WRF data for this release are from Ngan and Stein (2017). Even though observations exist beyond 48 hours, many of them are null in order to document the departure of the plume. Comparing the model SRM output to a small number of null observations results in degenerate STE solutions, so for this reason, the temporal sensitivity tests do not extend beyond 48 hours after the release.

Overall, the results in Table 9 show the SRM methodology struggles to obtain a reliable STE solution when observations are excluded beyond the initial release time, though several other trends are apparent. Higher resolution meteorological data provides green-coded solutions that can be obtained even if sampling is delayed six hours as shown in the WRF 9-km results. Also, the 0.5° SRM resolution provides the optimum results in each of the three meteorological files used. If a more precise solution is required, higher meteorological data may be required. CAPTEX 1 featured westerly

50

WRF 27-KM							
SRM Resolution	**ALL**	**≥6**	**≥12**	**≥18**	**≥24**	**≥36**	**≥48**
2°	red	red	red	red	red	red	red
1°	green	yellow	red	red	red	red	red
0.5°	green	yellow	yellow	red	red	red	red
0.25°	yellow	yellow	red	red	red	red	red
0.1°	green	yellow	yellow	red	red	red	red

WRF 9-KM							
SRM Resolution	**ALL**	**≥6**	**≥12**	**≥18**	**≥24**	**≥36**	**≥48**
2°	red	red	red	red	red	red	red
1°	green	yellow	yellow	yellow	yellow	red	red
0.5°	green	green	yellow	yellow	red	red	red
0.25°	green	green	red	red	yellow	red	red
0.1°	green	yellow	yellow	red	red	red	red

NARR 32.5-KM							
SRM Resolution	**ALL**	**≥6**	**≥12**	**≥18**	**≥24**	**≥36**	**≥48**
2°	red	red	red	red	red	red	red
1°	red	yellow	red	red	red	red	red
0.5°	yellow	yellow	yellow	red	red	yellow	red
0.25°	yellow	yellow	red	red	red	yellow	red
0.1°	green	yellow	red	red	red	red	red

Table 9. Reliability of the STE solution as observation times are excluded relative to the actual release time for CAPTEX 1. WRF data are from Ngan and Stein (2017). Results are color-coded according to Table 8.

flow that eventually transitioned to southerly flow in the later hours. Thus, excluding the early hours causes this transition to be lost in the observational record. This creates unreliability in the STE solution in later hours. Finally, the 0.5° and 0.25° SRMs in the NARR data yield yellow-coded solutions with 36 hours of observations excluded with red-coded solutions preceding and proceeding this test. This "improvement island" is misleading and likely an artifact of the color coding thresholds or general randomness in the model simulation, rather than a physical process occurring in the methodology. Therefore, for the rest of the study, no conclusions will be drawn from

(a)

(b)

(c)
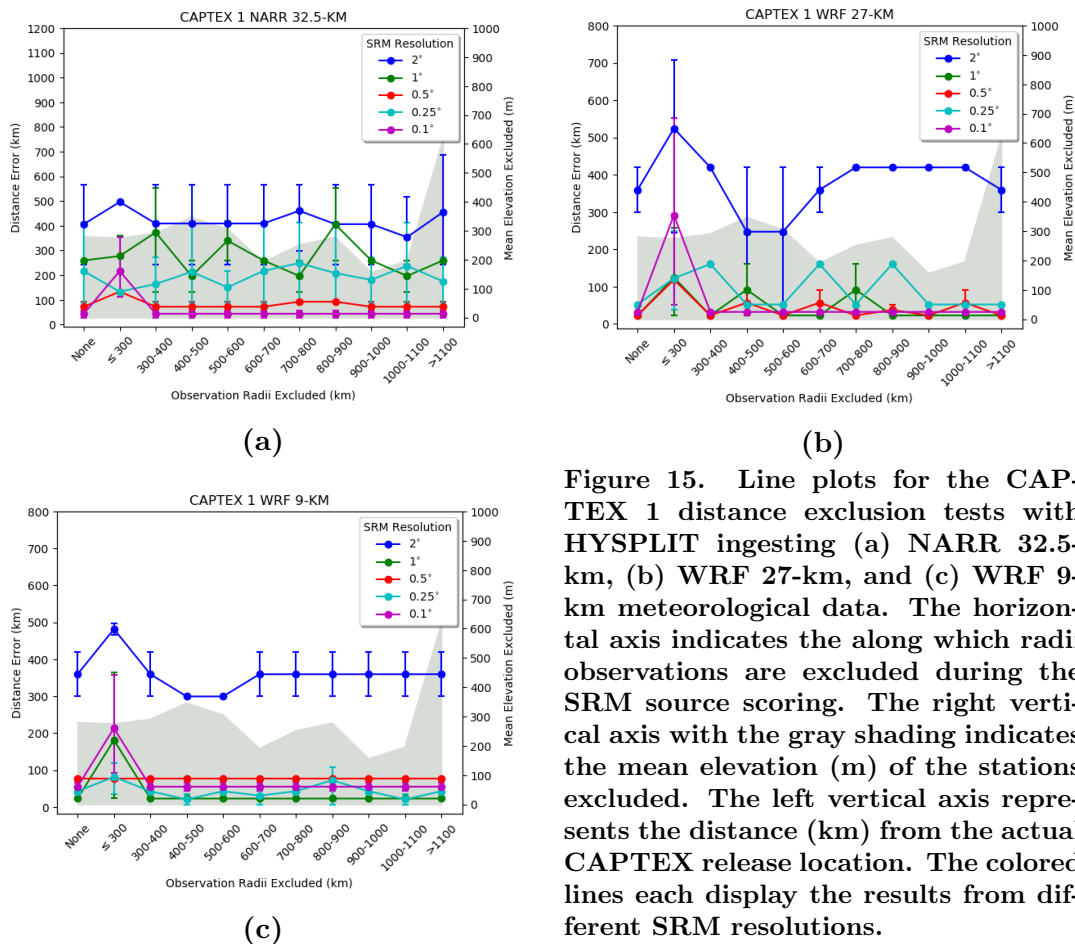
Figure 15. Line plots for the CAP-TEX 1 distance exclusion tests with HYSPLIT ingesting (a) NARR 32.5-km, (b) WRF 27-km, and (c) WRF 9-km meteorological data. The horizontal axis indicates the along which radii observations are excluded during the SRM source scoring. The right vertical axis with the gray shading indicates the mean elevation (m) of the stations excluded. The left vertical axis represents the distance (km) from the actual CAPTEX release location. The colored lines each display the results from different SRM resolutions.

these improvement islands in the time sensitivity tests.

The second sensitivity test assesses how the STE solution changes when observations at specified radii are removed from the comparison observation file. This test scores the sources within the SRM without using observations within the prescribed radius, mimicking a situation where these samplers are not available. As previously discussed, Figure 14 explains how the STE solution is represented in the line plots, and Figure 15 contains the plots for the distance sensitivity tests for CAPTEX 1. The horizontal axis indicates along which radii observations were excluded beginning with none and continuing in 100 km increments out to 1100 km. The right vertical axis represents the mean elevation of the stations excluded within the specified radii

and corresponds to the gray shading. The left vertical axis is the distance error of the STE solution. Each colored line represents a different SRM resolution. Each colored circle and whiskers display the STE solution for that SRM resolution scored with observations excluded at that corresponding radius indicated on the horizontal axis. Recall that the STE solution represents all modeled sources that scored within 0.1 model rank of the highest scoring source. The circle indicates the mean error of all these sources while the whiskers show the bounds of the farthest and closest sources within the STE solution. A circle with no whiskers—a sole-source solution—means no sources scored within 0.1 model rank of the highest scoring source, and the circle is the distance error of that highest scoring source.

As with the temporal sensitivity analysis for CAPTEX 1, the distance sensitivity analysis indicates that overall better STE solutions are obtained when ingesting higher resolution model data, as seen with the WRF 9-km data in Figure 15c. Not only does the mean distance error decrease, but the range of the distance error decreases or fully converges on a sole-source solution with the WRF 9-km meteorological data. Another signal evident in each meteorological case is the importance of the nearest observations less than or equal to 300 km away from the actual release location. Removing these observations for the majority of SRM resolutions increases both the mean distance error and the range of error. The 0.5° SRM resolution contains the most accurate solutions for the coarser meteorological files, but the 1° SRM outperforms the 0.5° with the 9-km resolution meteorological file. This means to obtain a more accurate solution, precision must be sacrificed in the form of coarser resolution SRM.

CAPTEX 2

CAPTEX 2 was released from Dayton, OH, at 1700 UTC on September 25, 1983. A high pressure center over the northeastern U.S. dominated the synoptic meteoro-

WRF 27-KM

SRM Resolution	Hours Included After Release						
	ALL	≥6	≥12	≥18	≥24	≥36	≥48
2°	yellow	yellow	yellow	green	green	green	red
1°	green	green	green	yellow	green	green	red
0.5°	green	green	green	yellow	green	yellow	red
0.25°	green	green	yellow	yellow	yellow	yellow	red
0.1°	green	green	yellow	yellow	red	red	red

WRF 9-KM

SRM Resolution	Hours Included After Release						
	ALL	≥6	≥12	≥18	≥24	≥36	≥48
2°	red	red	red	yellow	green	green	yellow
1°	green	green	green	yellow	yellow	red	yellow
0.5°	yellow	yellow	yellow	yellow	yellow	yellow	red
0.25°	green	green	green	yellow	yellow	yellow	red
0.1°	red	red	red	red	red	red	red

WRF 3-KM NESTED IN WRF 9-KM

SRM Resolution	Hours Included After Release						
	ALL	≥6	≥12	≥18	≥24	≥36	≥48
2°	yellow	yellow	yellow	yellow	green	green	red
1°	green	green	green	green	green	yellow	green
0.5°	green	green	green	yellow	yellow	yellow	red
0.25°	green	green	green	yellow	yellow	yellow	red
0.1°	green	green	green	red	red	red	yellow

NARR 32.5-KM

SRM Resolution	Hours Included After Release						
	ALL	≥6	≥12	≥18	≥24	≥36	≥48
2°	green	green	green	red	red	red	red
1°	green	green	green	red	red	yellow	red
0.5°	green	green	green	yellow	yellow	yellow	yellow
0.25°	green	green	green	yellow	yellow	yellow	yellow
0.1°	yellow	yellow	green	red	red	yellow	yellow

Table 10. Reliability of the STE solutions while excluding observations relative to the actual release time for CAPTEX 2. WRF 27-km and 9-km data are from Ngan and Stein (2017) (MYNN PBL scheme). WRF 3-km data is from the HYSPLIT Tutorial (YSU PBL scheme).

logical conditions. This meant the observed plume dispersed in lighter winds than in CAPTEX 1 and featured greater spatial plume extent. CAPTEX 2 is unique among the other CAPTEX releases in that analyses are performed using two sets of meteorological data: WRF data according to Ngan and Stein (2017) and WRF data used in the HYSPLIT Tutorial. The primary difference between these two sets are the PBL schemes where the former is MYNN and the latter is YSU (Ngan and Stein 2017; Air Resources Laboratory 2018a). The reliability of the STE solution as more time has elapsed before sampling begins is presented in Table 10. Sampling occurred as late as 58 hours after the release, but for the same reasons as stated previously, observation time periods are only excluded up to 48 hours. The WRF 27-km and 9-km meteorological files are obtained from Ngan and Stein (2017), but the WRF 3-km file is from the HYSPLIT Tutorial. This file only covers the state of Ohio and is nested within the WRF 9-km meteorological data.

The ability of the SRM approach to calculate a STE solution within $\pm 1°$ of the actual release location is improved over the results from CAPTEX 1. All four meteorological files provide green-coded STE solutions even after 12 hours have passed since the pollutant release when using SRM resolutions of $0.25°$ to $1°$. In this case, the 3-km meteorological data allows the same level of accuracy at 12 hours with the precision of a $0.1°$ resolution SRM. Additionally, the tests ingesting the WRF data indicate that coarser resolution SRMs of $1°$ to $2°$ allow for reliable solutions beyond 24 hours. While this may not provide a specific enough solution for some users, this suggests that it is still possible to narrow the source of a pollutant within a country or region, even if sampling does not begin until a day after the release occurred.

Next, Figure 16 presents the observational distance sensitivities for the same meteorological datasets. The marked increase in error when the observations less than 300 km away from the actual release location are removed highlights the importance

of the information those observations contain on the initial movement of the plume. One notable exception to this is the 2° SRM results for the WRF 9-km in Figure 16c, which shows a decrease in error when the closest observations are removed. This is because with a concentration grid of 2° resolution, those observations are in the same grid box as many of the sources closest to the actual release location. When the release begins in the HYSPLIT simulation, the plume instantaneously arrives at those observation locations within the concentration grid because they are in the same grid box. In reality, the plume takes a few hours to reach those location, so those sources score poorly. When those observations are removed, however, the scores of those sources increase, and they are included in the STE solution. This decreases the distance error of the STE solution. In summary, the decrease in error upon removal of near observations indicates the need to run a higher resolution SRM.

Similar to the CAPTEX 1 results, the 0.5° SRM provides the most consistent solutions across the meteorological files. Additionally, the most accurate solution of 26.4 km with these meteorological data is obtained with this SRM resolution. This is shown in Figure 16d, and this solution repeats across all radii exclusions except when the closest observations are excluded. This proves that increasing resolution at greater computation expensive does not guarantee a more accurate STE solution. In fact, the 0.1° SRM only consistently outperforms the coarser resolutions when the WRF 27-km data is ingested. The 0.1° SRM also shows sensitivity to elevation changes, especially in Figure 16c. As observations surrounding or located on higher terrain are removed, the average distance error decreases over the solution when all observations are taken into account. This indicates the difficulty when modeling dispersion near terrain features.

The SRM methodology is repeated on the CAPTEX 2 release only ingesting WRF data available within the HYSPLIT Tutorial, which utilizes the YSU PBL scheme

56
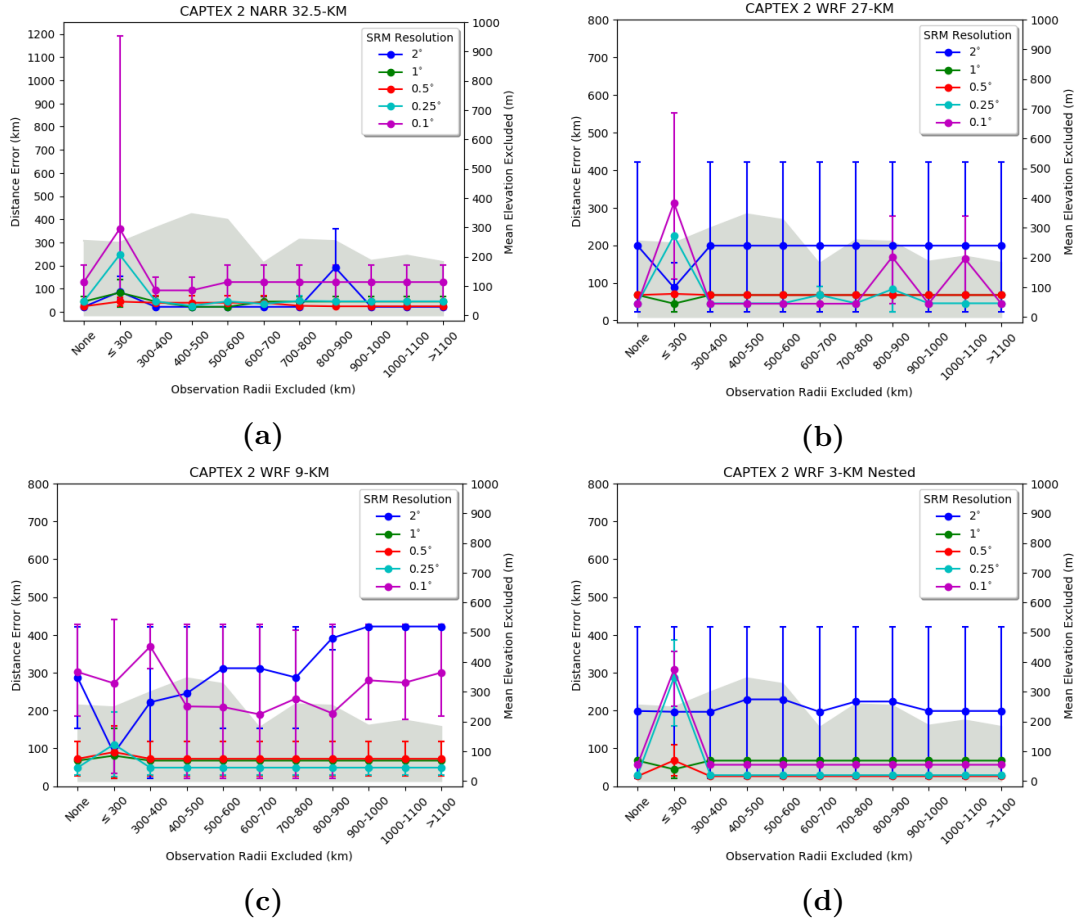
Figure 16. Line plots for the CAPTEX 2 distance exclusion tests with HYSPLIT ingesting (a) NARR 32.5-km, (b) WRF 27-km, (c) WRF 9-km, and (d) WRF 3-km nested within WRF 9-km meteorological data. The WRF 27-km and 9-km meteorological files are from Ngan and Stein (2017) using the MYNN PBL scheme, and the WRF 3-km file is from the HYSPLIT Tutorial, which uses the YSU PBL scheme. Data representation is identical to Figure 15.

(Air Resources Laboratory 2018a). Results illustrate how different parameterizations within the meteorological file significantly alter the STE outcome. Table 11 summarizes the results from the temporal sensitivity tests with the HYSPLIT Tutorial WRF data. With the exception of the 0.1° resolution SRM, no red-coded solutions are present for any sampling delay. Indeed, the WRF 27-km and 9-km allow reliable solutions with coarser SRM resolutions even after 48 hours has elapsed before observations begin. At the 0.1° SRM resolution, reliable solutions are calculated for all meteorological files even after 12 hours of observations are excluded. This shows

WRF 27-KM						
SRM Resolution	**ALL**	**≥6**	**≥12**	**≥18**	**≥24**	**≥36**	**≥48**
---	---	---	---	---	---	---	---
2°	yellow	yellow	yellow	yellow	green	green	yellow
1°	green	green	green	green	green	green	yellow
0.5°	green	green	green	green	green	green	green
0.25°	green	green	green	yellow	yellow	green	yellow
0.1°	green	green	green	red	red	red	yellow

WRF 9-KM						
SRM Resolution	**ALL**	**≥6**	**≥12**	**≥18**	**≥24**	**≥36**	**≥48**
---	---	---	---	---	---	---	---
2°	yellow	yellow	yellow	yellow	green	green	green
1°	green	green	green	green	green	green	green
0.5°	green	green	green	green	green	green	yellow
0.25°	green	green	green	green	yellow	yellow	yellow
0.1°	green	green	green	red	red	green	yellow

WRF 3-KM NESTED IN WRF 9-KM						
SRM Resolution	**ALL**	**≥6**	**≥12**	**≥18**	**≥24**	**≥36**	**≥48**
---	---	---	---	---	---	---	---
2°	yellow	yellow	yellow	green	green	green	yellow
1°	green	green	green	green	green	yellow	green
0.5°	green	green	yellow	yellow	yellow	green	yellow
0.25°	green	yellow	green	green	green	green	yellow
0.1°	green	green	green	yellow	red	yellow	yellow

Table 11. Reliability of the STE solutions while excluding observations relative to the actual release time for CAPTEX 2. All WRF data are from the HYSPLIT Tutorial, which uses the YSU PBL scheme.

improvement over the solutions obtained with the Ngan and Stein (2017) WRF files where 3-km meteorological file resolution is required to obtain similar results.

The HYSPLIT Tutorial WRF tests also show several improvements in the distance sensitivity results shown in Figure 17. While the 1°, 0.5°, and 0.25° SRM resolutions show similar results across the WRF resolutions as compared to the previous results in Figure 16, the 2° and 0.1° SRM resolutions show improvements in mean distance error and range of error. Additionally, elevation changes cause less volatility in the STE solution at these resolutions. This indicates parameterizations in the HYSPLIT

(a)

(b)

(c)
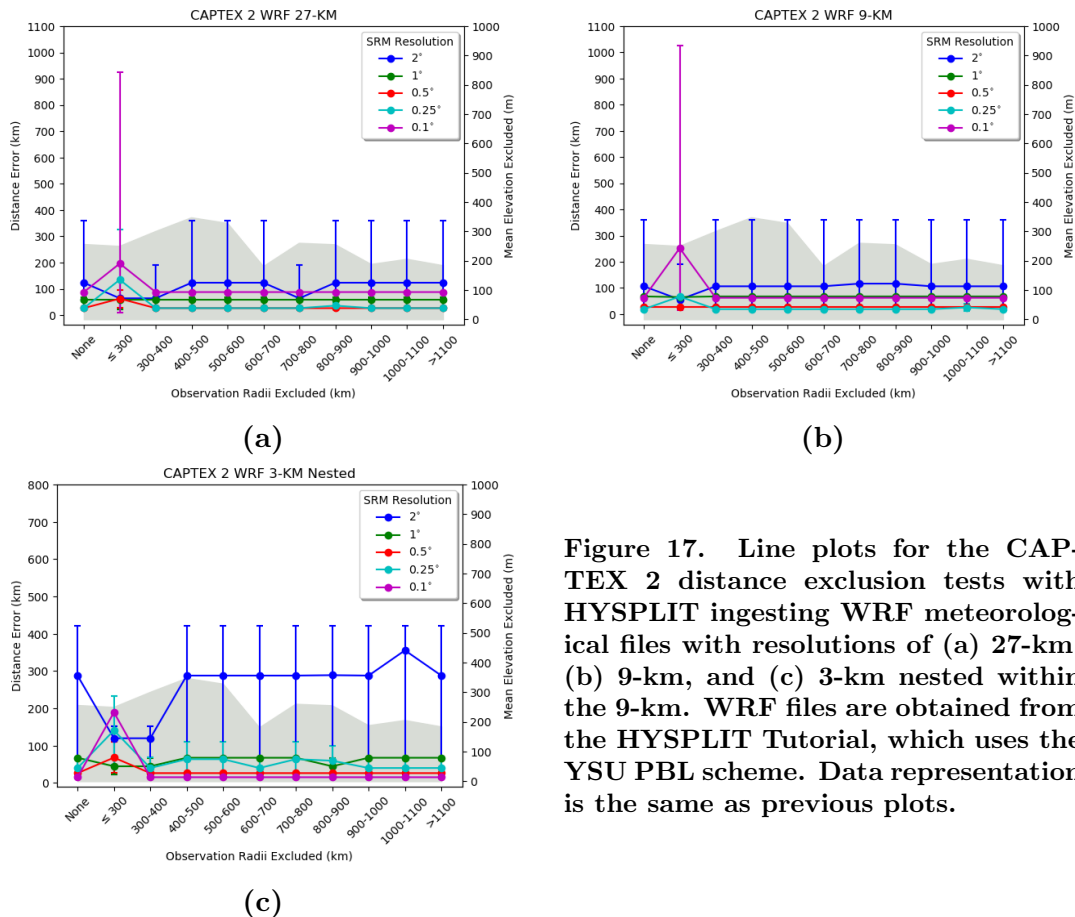
Figure 17. Line plots for the CAP-TEX 2 distance exclusion tests with HYSPLIT ingesting WRF meteorological files with resolutions of (a) 27-km, (b) 9-km, and (c) 3-km nested within the 9-km. WRF files are obtained from the HYSPLIT Tutorial, which uses the YSU PBL scheme. Data representation is the same as previous plots.

Tutorial WRF allow HYSPLIT to simulate the dispersion physics near terrain more accurately. The 2° SRM resolution does increase in mean distance error with the WRF 3-km meteorological data in Figure 17c. This indicates that increasing the meteorological data resolution does not necessarily benefit the STE solution if the SRM resolution remains coarse.

CAPTEX 3

CAPTEX 3 is the next pollutant release this study applies the SRM methodology to calculate STE solutions. This release also originated at Dayton, OH and occurred at 1900 UTC on October 2, 1983. The meteorological conditions carried the original plume northeastward into Canada before moving east over the state of New York.

59

WRF 27-KM

SRM Resolution	Hours Included After Release						
	ALL	≥6	≥12	≥18	≥24	≥36	≥48
2°	red	red	red	red	yellow	green	red
1°	green	green	yellow	yellow	yellow	red	green
0.5°	yellow	yellow	yellow	yellow	yellow	red	red
0.25°	yellow	yellow	yellow	red	red	red	red
0.1°	green	green	yellow	yellow	yellow	yellow	yellow

WRF 9-KM

SRM Resolution	Hours Included After Release						
	ALL	≥6	≥12	≥18	≥24	≥36	≥48
2°	red	red	red	red	red	yellow	red
1°	yellow	yellow	yellow	red	red	red	red
0.5°	yellow	yellow	red	red	red	red	red
0.25°	green	green	yellow	yellow	red	red	yellow
0.1°	yellow	yellow	red	red	red	red	yellow

NARR 32.5-KM

SRM Resolution	Hours Included After Release						
	ALL	≥6	≥12	≥18	≥24	≥36	≥48
2°	red	red	red	red	yellow	red	red
1°	yellow	red	yellow	red	red	red	red
0.5°	yellow	yellow	red	red	yellow	red	red
0.25°	green	green	red	red	yellow	yellow	red
0.1°	yellow	yellow	yellow	green	yellow	yellow	red

Table 12. Reliability of the STE solutions while excluding observations relative to the actual release time for CAPTEX 3. The WRF data are obtained from Ngan and Stein (2017).

Ferber et al. (1986) noted that a portion of the plume was cutoff aloft by stabilization taking place in the afternoon. The plume mixed down the morning following the release as downstream samplers recorded an increase in concentration values. As with CAPTEX 1, WRF meteorological data from Ngan and Stein (2017) and the NARR are ingested into HYSPLIT for the CAPTEX 3 sensitivity analyses. Observation stations reported concentrations out to 65 hours following the release, but just as with the previous tests, the temporal sensitivity only excludes observations up to 48 hours after the release. Both the temporal and observational distance sensitivity tests

utilize SRM resolutions of 2°, 1°, 0.5°, 0.25°, and 0.1°.

First, the temporal reliable of the STE solution is shown in Table 12. The overall reliability regardless of meteorological file and SRM resolution is decreased when contrasted to the results from CAPTEX 2. In fact, these results are similar to the reliability results that are obtained from the CAPTEX 1 release in Table 9. As the methodology and meteorological models ingested are the same for both the CAPTEX 1 and 3 releases, this indicates similarities in the meteorological data cause less reliability in the STE solution than in the meteorology data for CAPTEX 2. Both CAPTEX 1 and 3 feature shifts of westerly flow to southerly flow causing the observed plume to shift from moving longitudinally to latitudinally. If the hours that this shift occurred are removed from the comparison observation file, this information is lost to the SRM methodology at the cost of the accuracy of the STE solution. Thus, changing mean wind flow conditions may limit the allowable sampling delay to obtain a reliable solution.

In addition, the 2° SRM resolution performs unreliably in all meteorological datasets. Other trends are not as apparent. Both the 1° and 0.1° perform well up to 6 hours of excluded observations in the WRF 27-km dataset. In this case, a coarse and fine resolution SRM obtained reliable solutions, but not the two intermediate SRM resolutions. The 0.25° resolution SRM does show improvement in both finer resolution (WRF 9-km) and coarser (NARR 32.5-km) meteorological datasets, however. The clearest trend is that for this CAPTEX release, if sampling would have begun after 6 hours post-release, a obtaining a reliable STE solution would be difficult regardless of meteorological data or SRM resolution used.

Next, Figure 18 summarizes the results from the observational distance sensitivity test for CAPTEX 3. As previously observed in the CAPTEX 2 results, applying a higher resolution SRM with higher resolution meteorological input does not neces-
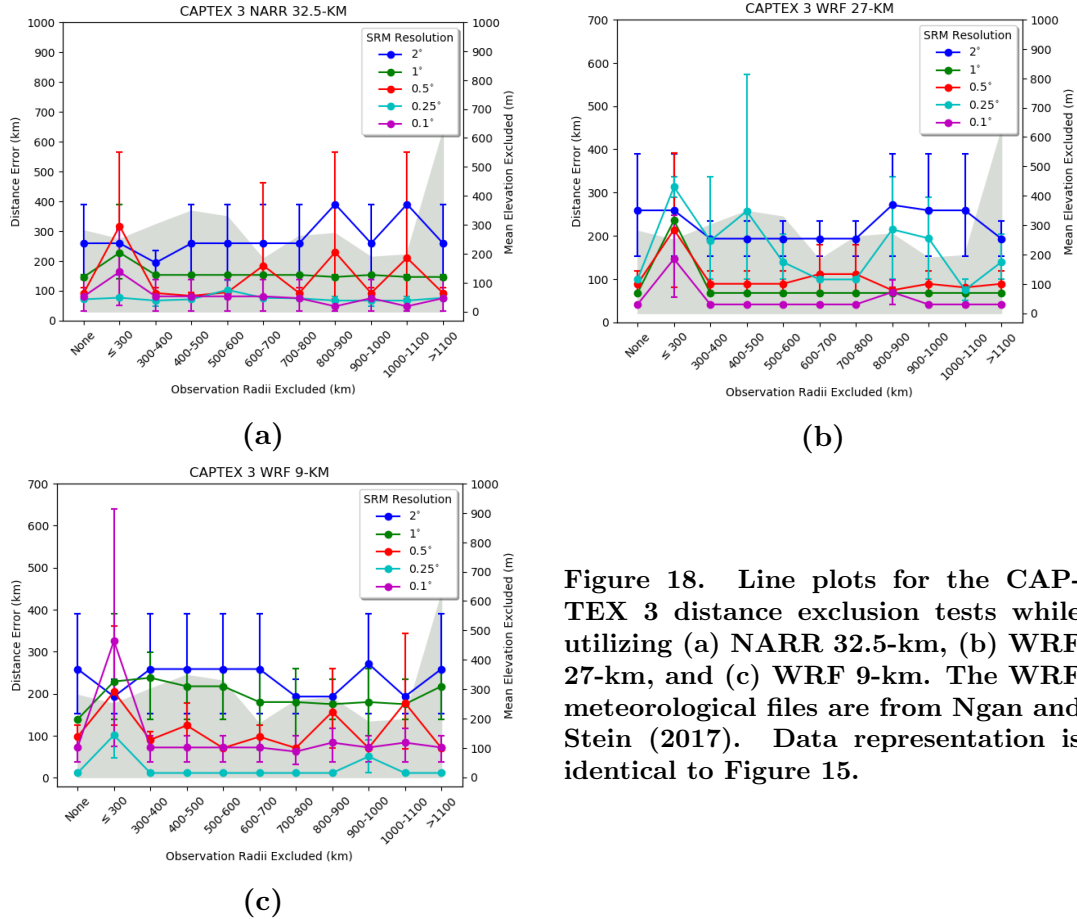
Figure 18. Line plots for the CAPTEX 3 distance exclusion tests while utilizing (a) NARR 32.5-km, (b) WRF 27-km, and (c) WRF 9-km. The WRF meteorological files are from Ngan and Stein (2017). Data representation is identical to Figure 15.

sarily result in a more accurate STE solution. For example, the 0.1° SRM with the NARR meteorological data in Figure 18a provides a solution with a mean distance error as small as 47.2 km. However, when ingesting the WRF 9-km data shown in Figure 18c the solution with the smallest mean distance error increases to 62.2 km. CAPTEX 3 featured less synoptically forced meteorological conditions similar to CAPTEX 2, therefore, these results show that modeling random dispersion at high resolutions is difficult and can cause greater error STE solutions.

Focusing only on the two WRF-utilizing tests, a dramatic improvement in the performance of the 0.25° SRM is noted. This SRM resolution consistently provides the second worst STE solutions in the WRF 27-km tests while consistently providing solutions with the lowest distance error in the WRF 9-km tests. Indeed, the 11.4 km

error sole-source solution shown in Figure 18c is among the best solutions calculated by this methodology for all CAPTEX releases. Determining why is difficult without further testing, but clearly for these meteorological conditions the WRF-ingesting HYSPLIT simulation is optimizing at the 0.25° SRM resolution.

Other trends are similar to ones noted from previous CAPTEX releases. The observations obtained within 300 km remain vital to calculating an accurate STE solution. The only exception to this is the 2° SRM with the WRF 9-km data for the reason previous discussed. The 0.5° SRM resolution performs consistently across all meteorological datasets, though it does not provide the most accurate results for this release. The improvement in the STE solution when removing observations in proximity to higher terrain appears in the 0.1° resolution SRM using the NARR data when the 800-900 km and 1000-1100 km observations are removed.

CAPTEX 4

The CAPTEX 4 release was conducted on October 14, 1983 beginning at 1600 UTC from Dayton, OH. The meteorological conditions featured a tight westerly gradient that quickly transport the original plume east over southern Pennsylvania and New Jersey, confining the plume to a narrow corridor. The sampling stations recorded observations up to 53 hours following the beginning of the release, and as with the previous releases, the temporal sensitivity test excludes observations only as late as 48 hours after the release. The WRF data is utilized from Ngan and Stein (2017), and SRM resolutions of 2°, 1°, 0.5°, 0.25°, and 0.1° are tested.

First, the results from the temporal reliability of the STE solution are given in Table 13. Only the 0.5° SRM resolution provides reliable solutions across all three meteorological files, though observations are required no later than six hours after the release. Higher resolution SRMs do not show more reliability regardless of the meteo-

63

WRF 27-KM

SRM Resolution	ALL	≥6	≥12	≥18	≥24	≥36	≥48
2°	yellow	yellow	green	red	red	red	red
1°	yellow	green	yellow	red	red	red	red
0.5°	green	green	red	yellow	red	red	red
0.25°	yellow	yellow	red	yellow	red	red	red
0.1°	yellow	yellow	red	red	red	red	red

WRF 9-KM

SRM Resolution	ALL	≥6	≥12	≥18	≥24	≥36	≥48
2°	yellow	yellow	yellow	red	red	red	red
1°	green	green	red	red	red	red	red
0.5°	green	green	red	yellow	red	red	red
0.25°	yellow	yellow	yellow	red	red	red	red
0.1°	yellow	yellow	red	red	red	red	red

NARR 32.5-KM

SRM Resolution	ALL	≥6	≥12	≥18	≥24	≥36	≥48
2°	green	green	red	red	red	red	red
1°	yellow	yellow	yellow	yellow	red	red	red
0.5°	green	green	yellow	yellow	red	red	red
0.25°	yellow	yellow	yellow	yellow	red	red	red
0.1°	green	green	yellow	yellow	red	red	red

Table 13. Reliability of the STE solutions while excluding observations relative to the actual release time for CAPTEX 4. The WRF data are obtained from Ngan and Stein (2017).

rological model ingested. This contrasts with CAPTEX 3 where reliable solutions are obtained at the 0.25° and 0.1° resolutions under certain conditions. Also, the meteorological conditions coupled with the performance of HYSPLIT for the CAPTEX 4 release do not show any level of reliability beyond 18 hours of observation exclusion. This is the most restrictive result in this regard to this point. This could be due to the fact that the actual plume followed a wind band over Pennsylvania and dispersed over the ocean beyond 18 hours. No observations were taken over the ocean so very little information regarding the plume dispersion is available to calculate the solution

when the earliest observations are disregarded.

The sensitivity of the STE solution to observational distance is subsequently shown in Figure 19 for CAPTEX 4. As seen in previous results, the necessity of observations within 300 km of the actual release location is apparent in each sub-figure. In contrast with the results from the previous CAPTEX releases, the coarser resolution SRMs exhibit less distance error and uncertainty than the finer resolution SRMs. The $2°$ and $1°$ resolution SRMs consistently result in distance errors below 50 km while the $0.25°$ and $0.1°$ resolutions obtain solutions with errors above 100 km. This trend is independent of meteorological data resolution as the finer resolution SRMs perform worse than the coarser resolution SRMs across all meteorological file resolutions. The $0.5°$ resolution SRM provides consistent solutions with errors between 50 km and 100 km across all meteorological inputs.

The meteorological conditions noted in the temporal sensitivity analysis may also explain the poor performance of the finer resolution SRMs. As the plume quickly dispersed over the ocean, the SRM methodology is left with null observations in the later sampling periods. This means the model rank calculation is only comparing areas where the plume does not exist in the observational record to areas where the plume does not exist in the HYSPLIT simulations. This allows many of the sources tested to score well, as the area free of the plume is larger than the area covered by the plume. Since the higher resolution SRMs contain more possible sources within their source grids, this increases the possibility that these incorrect, but high scoring sources contaminate the resulting STE solution. This highlights the importance of ingesting non-zero concentration observations into this methodology to ensure the possible sources are scored based on where the plume exists and not where it does not.

(a)

(b)

(c)
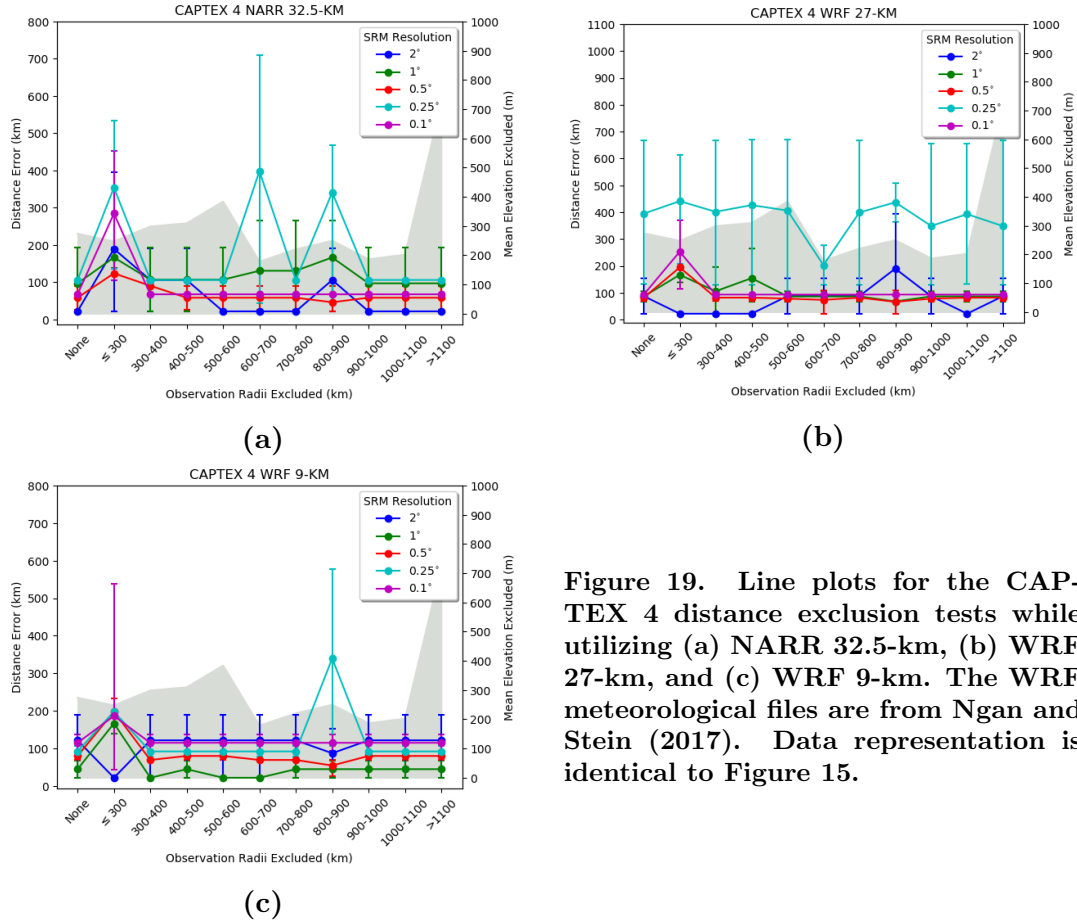
Figure 19. Line plots for the CAP-TEX 4 distance exclusion tests while utilizing (a) NARR 32.5-km, (b) WRF 27-km, and (c) WRF 9-km. The WRF meteorological files are from Ngan and Stein (2017). Data representation is identical to Figure 15.

CAPTEX 5 and 7

CAPTEX 5 and 7 are the last two CAPTEX releases tested with the SRM methodology in this study. The CAPTEX 5 release began on October 26, 1983 at 0400 UTC, and CAPTEX 7 was released on October 29, 1983 at 0600 UTC. Both releases initiated from Sudbury, ON and were released behind cold fronts in northwesterly flow. The meteorological conditions were similar for both releases, though the higher wind speeds featured in CAPTEX 7 resulted in faster plume transport through the network. The performance of the methodology in obtaining STE solutions is similar for both releases to the results presented for CAPTEX 1-4. The reliability of the methodology shows sensitivity to the nearest observations in both time and space, removal of observations within higher terrain reduces the mean distance error, and

66

the 0.5° SRM continues to be the least sensitive resolution to changes in meteorological data and conditions. The tables and plots for both releases are available in Appendix B. For CAPTEX 5, Table 17 contains the reliability of the STE solutions for the temporal exclusion tests, and Figure 26 displays the results from the distance exclusion tests. Likewise, for CAPTEX 7, Table 18 shows the temporal exclusion results, and Figure 27 depicts the distance sensitivity plots.

Results: Nuclear Detonation Cases (NUDETs 1951-1957)

Extending the methodology created from the robust CAPTEX data, the SRM methodology is modified to solve for the source locations of two nuclear detonation tests that occurred at the NTS named Simon and Smoky. As previously discussed, each source requires its own distinct HYSPLIT simulation due to the complexity of modeling a stabilized nuclear cloud. Both cases presented ingest the WRF 12-km meteorological data from Rolph et al. (2014). This resolution, the finest available, is utilized due to the finer resolutions chosen for the NUDET SRMs compared to the CAPTEX SRMs. As noted above, finer resolution meteorological data coupled with finer resolution SRMs does not always minimize error in the STE solution in less synoptically forced meteorological conditions, such as light and variable low level winds under high pressure. However, the CAPTEX results also showed that finer resolution meteorological data and SRMs can improve the STE solution when pollutants are confined within a narrow corridor in strong synoptic forcing. Since most of the particles within the stabilized nuclear cloud are transported in mid-to-upper tropospheric flow exceeding 25 kts, the higher resolutions that benefit the STE outcome apply in these meteorological conditions.
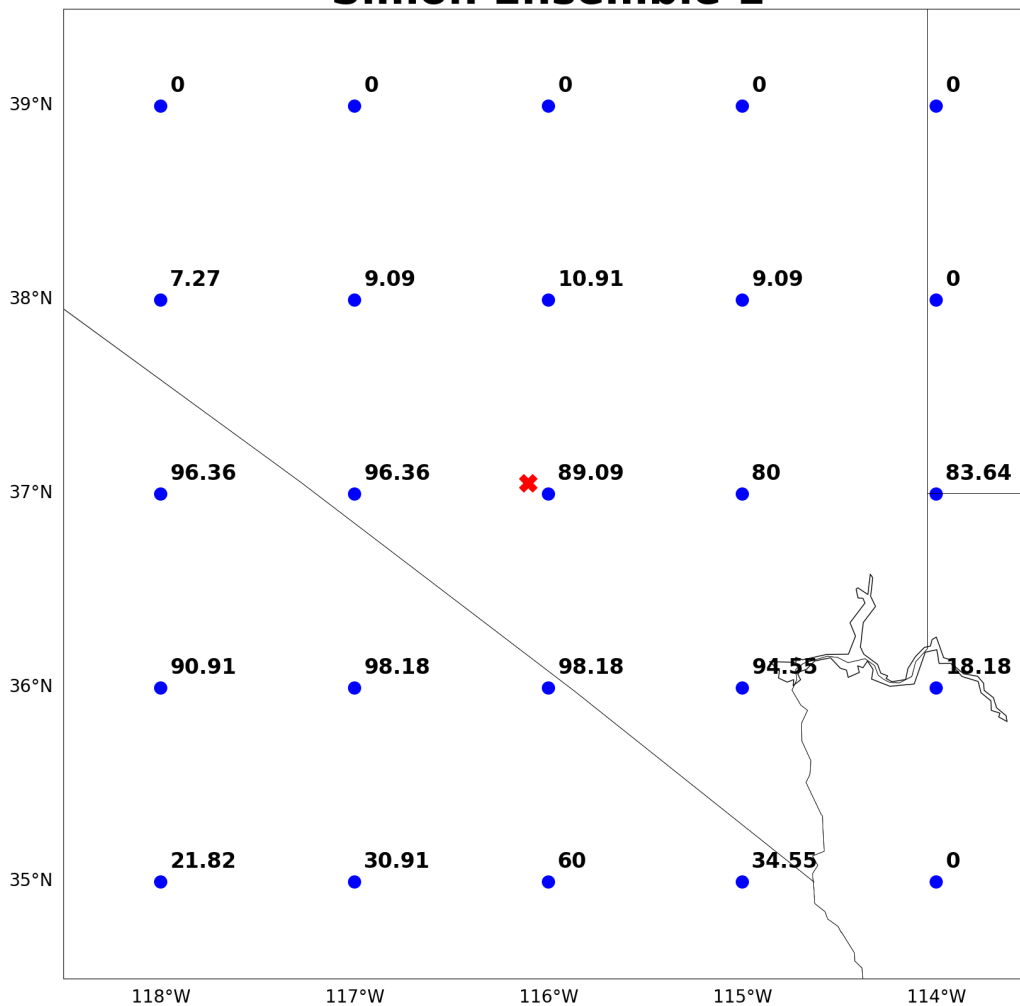
Figure 20. Results from the first ensemble of the Simon simulations. Each blue circle is a source location that is tested with the resulting FMS displayed adjacently. The red "X" shows the actual location of the Simon detonation.

Simon Nuclear Detonation

The Simon nuclear detonation test occurred on April 25, 1953 at 1200 UTC at the NTS and is regarded as the most spatially accurate HYSPLIT simulation (Rolph et al. 2014). First, HYSPLIT is ran from each source depicted on Figure 13 and configured as specified in the previous chapter. The SRM methodology is modified to decouple the resolutions of the source grid and the concentration grid within HYSPLIT. This first test utilizes a 1° resolution source grid and a 0.1° resolution concentration grid.

Figure 21. Results from the second ensemble of the Simon simulations. Each circle is a source location within the ensemble. The shading indicates the model rank of the simulation of that source. The model rank is multiplied by 100 to increase separation in the color shading. The red "X" shows the actual location of the Simon detonation.

Figure 20 presents the FMS results from each of the sources within the first ensemble of Simon simulations. Sources with higher FMS scores indicate origin locations where HYSPLIT replicates the spatial distribution of the observed dosage plume. At this resolution, the model rank metric discriminates against too many sources specifying too little area for the next finer-resolution ensemble. Thus, the FMS metric is chosen over the model rank to indicate from which region the next finer-resolution ensemble should be initialized. For this first ensemble, the highest FMS is 98.18 scored by two sources located 141.8 km and 117.2 km away from the true detonation location.

The second ensemble source grid domain is determined from the sources in the first ensemble with FMS scores ≥90. This results in a source grid spanning 36-37°N and 115-118°W. The source grid utilizes a 0.1° resolution and the concentration grid resolution is set to 0.05°. Since the FMS is used to determine the domain of the second ensemble, all sources exhibit high FMS metrics and this does not discriminate enough to narrow down the domain for the next ensemble. Therefore, the model rank of each source is compared to determine which region replicates the actual dose rate values within HYSPLIT. Figure 21 displays the results of the second ensemble.
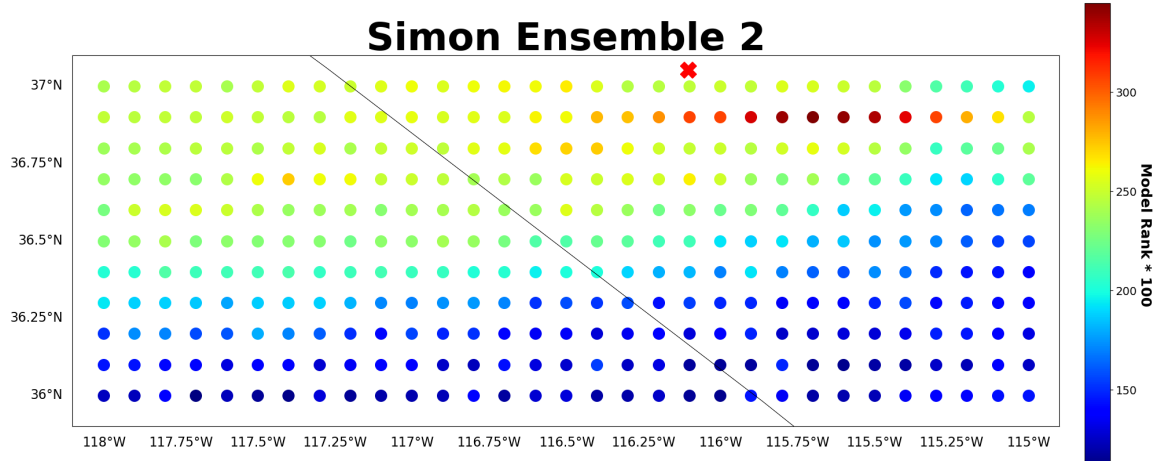
Figure 22. Results from the third ensemble of the Simon simulations. Each circle is a source location within the ensemble. The shading indicates the model rank of the simulation of that source. The model rank is multiplied by 100 to increase separation in the color shading. The red "X" shows the actual location of the Simon detonation.

The STE solution contains four sources scoring within 0.1 model rank of the highest scoring source. These sources are shaded dark red in the figure. The closest of these sources to the actual detonation location has a distance error of 31.9 km, and the mean distance error of the four sources within the STE solution is 43.9 km. At this point, this methodology is focusing the STE solution to the southeast of the actual detonation location.

The domain of the third Simon ensemble focuses on an area surrounding the four highest scoring sources from the second ensemble. This next source grid contains 55 sources at 0.05° resolution spanning 36.8-37°N and 115.5-116°W. The concentration grid resolution is increased to 0.01°. As with the previous ensemble, model rank is selected as the metric to compare the performance of the sources. Figure 22 displays the resulting model rank from each source within the third ensemble. The STE solution only encompasses one source as no other sources scored within 0.1 model rank. This sole-source solution has a distance error of 21.8 km to the southeast of the
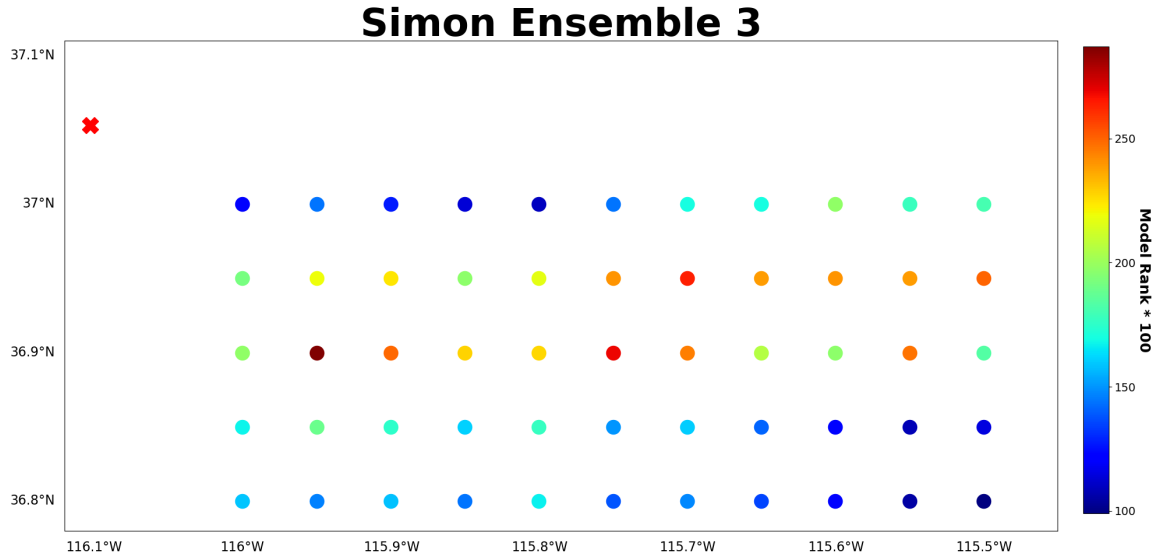
70
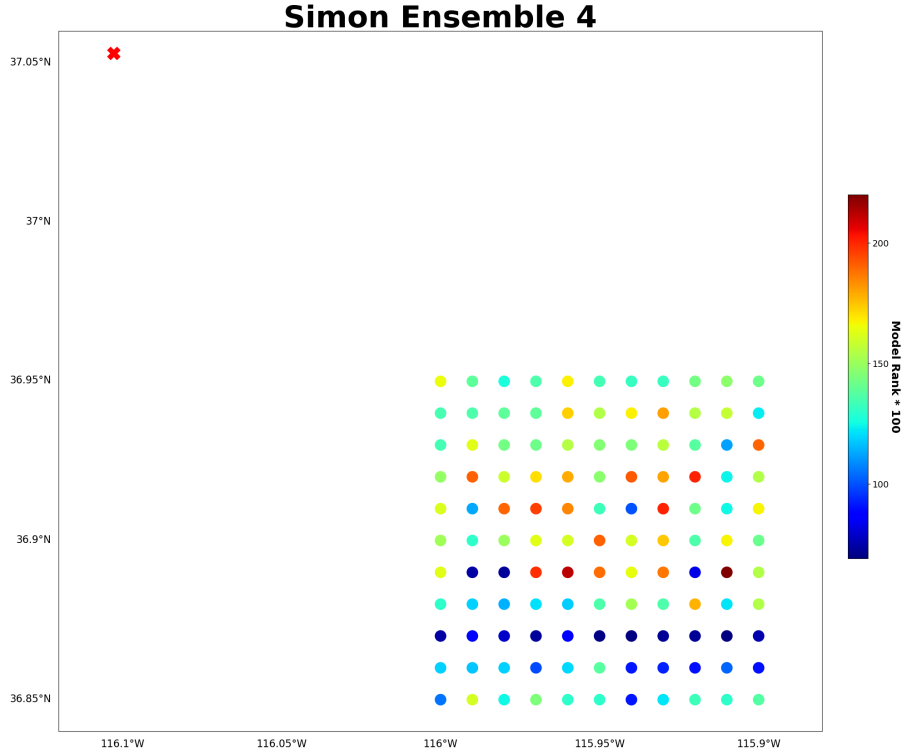
Figure 23. Results from the fourth ensemble of the Simon simulations. Each circle is a source location within the ensemble. The shading indicates the model rank of the simulation of that source. The model rank is multiplied by 100 to increase separation in the color shading. The red "X" shows the actual location of the Simon detonation.

actual Simon detonation. Figure 22 shows that this source is located on the western edge of the source grid used to create the ensemble members, thus, a fourth ensemble is conducted to see if the solution keeps converging westward, which would minimize the distance error.

The fourth and final ensemble that is conducted with the Simon data is the finest resolution source and concentration grid tested at $0.01°$ and $0.005°$, respectively, containing 121 ensemble members. As before, the domain spans around the preceding highest performing source at 36.85-$36.95°$N and 115.9-$116°$W. The results from this final ensemble are shown in Figure 23. The STE solution contains two sources within 0.08 model rank located 22.1 and 24.4 km away from the true detonation site resulting in a mean distance error of 23.5 km. This solution is worse than the solution of the

71

Simon Detonation Summary						
Ensemble	Source Grid Domain	Source Grid Resolution	# of Sources	Concentration Grid Resolution	STE Solution Mean Distance Error (km)	STE Solution Least Distance Error (km)
1	35-39°N, 114-118°W	1°	25	0.1°	144.5	80.05
2	36-37°N, 115-118°W	0.1°	341	0.05°	43.9	31.9
3	36.8-37°N, 115.5-116°W	0.05°	55	0.01°	21.8	21.8
4	36.85-36.95°N, 115.9-116°W	0.01°	121	0.005°	23.5	22.1

Table 14. Summary of the ensemble makeups and results of the Simon NUDET.

preceding ensemble, though these sources are within the source grid resolution of the previous ensemble. Since the solution did not continue to converge towards the true detonation location, the higher resolution ensemble does not provide further improvement in the STE outcome. Therefore, no further ensembles are conducted utilizing the Simon detonation data. The third ensemble provides the STE solution with the least distance error of 21.8 km. Table 14 summarizes the results of the ensembles tested with the Simon data.

Smoky Nuclear Detonation

To understand the other extreme, the SRM methodology is applied to Smoky: a NUDET ranked with the worst HYSPLIT FMS score in the Rolph et al. (2014) study. This allows analysis on the importance of the accuracy of the HYSPLIT simulation itself by comparing the Smoky STE results to the Simon STE results, which was the best performing NUDET case in Rolph et al. (2014). The first ensemble of the Smoky case utilizes the same initial 1° resolution source grid as the Simon case as depicted in Figure 13, previously. Also, the same 0.1° concentration grid is set for each member. The results of the FMS scores for each source within this ensemble are shown in Figure 24. Only two sources score an FMS value higher than zero with a highest FMS score of 80. This contrasts with the first ensemble of Simon that had multiple source score above 90. This means even the best scoring sources in the Smoky ensemble are not replicating the spatial dose rate distribution as well as the Simon ensemble, which correlates with the results noted in Rolph et al. (2014).
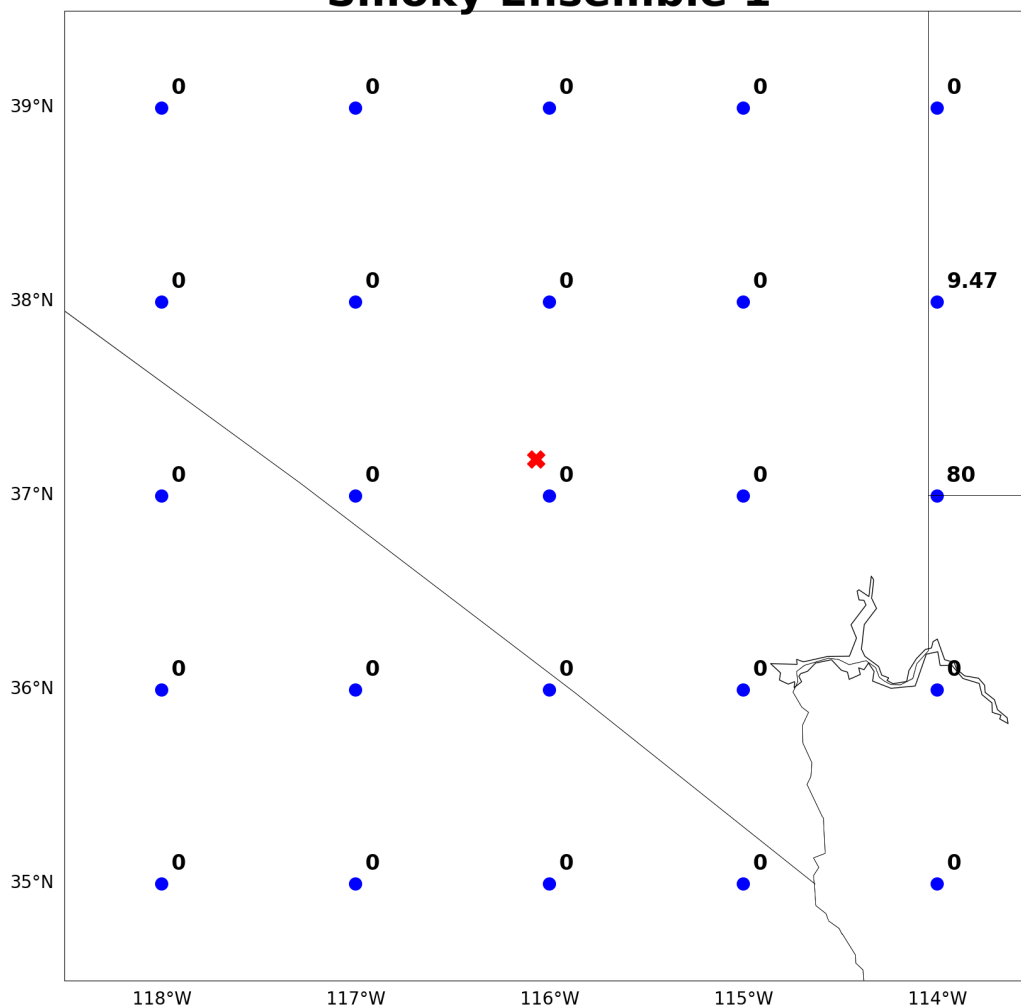
Figure 24. Results from the first ensemble of the Smoky simulations. Each blue circle is a source location that is tested with the resulting FMS displayed adjacently. The red "X" shows the actual location of the Smoky detonation.

Nevertheless, the area surrounding these two nonzero FMS-scoring sources is tested at a higher resolution for the second Smoky ensemble.

The second Smoky ensemble includes 176 sources spanning 36.5-38°N and 113.5-114.5°W that results in a source grid resolution of 0.1°. The concentration grid resolution in this ensemble is increased to 0.05° to be consistent with the resolution of the second Simon ensemble. As with the Simon NUDET, the model rank is adopted as the metric for scoring the performance of the second ensemble members, and Figure 25
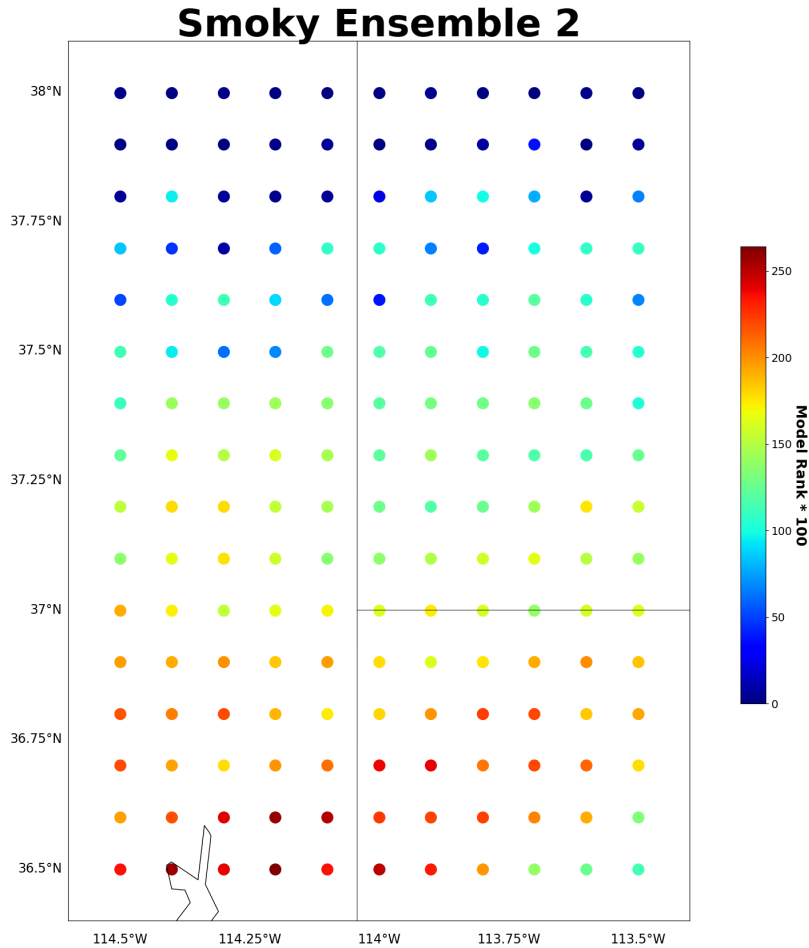
Figure 25. Results from the second ensemble of the Smoky simulations. Each circle is a source location within the ensemble. The shading indicates the model rank of the simulation of that source. The model rank is multiplied by 100 to increase separation in the color shading. The actual detonation location is not pictured and located to the west of the ensemble domain.

displays the results. The STE solution for this ensemble contains three sources with a mean distance error of 176.4 km. The sources are clustered near the southeastern portion of the source grid, which is due east of the actual detonation location. It is known from the previous ensemble, that sources farther west and closer to the true detonation location will likely not score well as their FMS scores are not above zero. Thus, no further ensemble testing is conducted because the Smoky case clearly yields a STE solution with higher error than the Simon case. Table 15 summarizes the results of both ensembles conducted with the Smoky data. The poorer performance

Smoky Detonation Summary						
Ensemble	Source Grid Domain	Source Grid Resolution	# of Sources	Concentration Grid Resolution	STE Solution Mean Distance Error (km)	STE Solution Least Distance Error (km)
1	35-39°N, 114-118°W	1°	25	0.1°	194.3	185.0
2	36.5-38°N, 113.5-114.5°W	0.1°	176	0.05°	176.4	167.2

Table 15. Summary of the ensemble makeups and results of the Smoky NUDET.

of HYSPLIT in this case, while still able to provide a STE solution within 200 km, does affect the ability of this methodology to minimize the distance error in the STE solution.

Summary

This chapter presented the results of the SRM methodology on two different types of datasets. First, the SRM methodology was tested on the CAPTEX data. This provided multiple cases to test the effectiveness of the methodology in different meteorological conditions. Additionally, the reliability of the STE solution as sampling is delayed from the release time was evaluated along with the sensitivity of the solution to observations at different distances. Second, two NUDET cases in 1953 and 1957 provided another type of dataset to test the methodology, which was modified into a true ensemble where the source locations served as the ensemble members. The ability of HYSPLIT to more accurately simulate the dispersion of the dose rate plume in the Simon case ultimately allowed for a more accurate STE solution compared to the Smoky case. The next chapter discusses the significance of these findings and proposes future work to expand on them.

V. Conclusions

The main purpose of this research was to determine if a methodology incorporating an ensemble of forward HYSPLIT concentrations where the source location is varied provides a viable STE solution of atmospheric pollutants. The results presented in Chapter IV demonstrated the capability of this concept in several datasets dealing with a one source of emission with multiple concentration receptors.

Findings: CAPTEX 1983

First, Chapter IV Section Results: CAPTEX 1983 demonstrated a SRM with the CAPTEX data in order to take advantage of computational efficiencies within HYS-PLIT, specifically the ability to simulate all of the releases of the sources in one iteration of HYSPLIT. The CAPTEX dataset provided varied meteorological conditions across the synoptic scale in order to test the SRM effectiveness of the methodology. Some cases, such as CAPTEX 2 and 3, were less synoptically forced in that lower wind speeds and less defined wind bands allowed the plume to disperse more randomly in all directions, such as the case with high pressure. *Since HYSPLIT struggled to explicitly simulate random dispersion at higher resolutions, inputting higher resolution meteorological data did not necessarily decrease the distance error in the STE solution.* The other releases contained meteorological conditions with higher wind speeds confined in well-defined gradients. HYSPLIT is better able to explicitly simulate the plume dispersion in these scenarios, therefore, higher resolution meteorological data and SRMs decreased distance error in the STE solution. As running HYSPLIT with higher resolution meteorological data with higher resolution SRMs requires greater computational expense, it is important to understand the meteorological conditions of the dispersion environment at hand to determine whether devoting greater computing

resources will yield better results.

The CAPTEX trials also featured both temporal and spatial sensitivity analyses by removing specific observations in order to investigate the change in the STE solution. *All CAPTEX releases showed that a reliable STE solution can be obtained as long as sampling began no later than 6 hours after the actual release.* The ability to maintain reliability beyond that point required that enough positive concentration observations be available in the later hours. The solution degenerates if the methodology is only given concentration observations of zero to compare to the SRM concentration values. Also, if shifts in the meteorological pattern occur, such as predominant westerly flow changes to southerly flow as occurred during the CAPTEX 1 and 3 releases, sampling observations must exist during the period of changing flow regimes otherwise this information is lost to the methodology and reliable STE solutions cannot be obtained.

Next, the spatial sensitivity tests revealed two trends that should be considered when developing a sampling strategy for an atmospheric contaminant event. *First, removing the observations nearest to the actual release location introduces the most distance error and uncertainty into the STE solution, which emphasizes the importance of these observations.* In the case of CAPTEX, the error in the solution showed the greatest sensitivity to the observations within 300 km of the actual release location. *Second, several instances pointed to observations surrounding or located on elevated terrain contaminating the observational dataset as their removal prompted a decrease in the distance error of the STE solution.* This points to the difficulty in simulating dispersion in vertical turbulence in orographic lift regions. Comparing the poor performance of the model in these regions to the actual observations artificially lowers the performance of certain sources within the SRM, thus causing other sources farther away from the actual release location to score higher by default. This

is how error is introduced into the STE solution. Therefore, when sampling an area contaminated with an airborne pollutant, these results suggest focusing on sampling areas with less terrain and more well-defined mesoscale flow, as sampling areas with orographic lift may not add to, or may even subtract from, the accuracy of the STE solution.

The last conclusion drawn from the CAPTEX data is that the parameterizations selected in the meteorological model preceding HYSPLIT are a main source of error in the STE solution. *Specifically, the PBL schemes utilized significantly changed the STE outcome in the CAPTEX 2 trials even at higher resolutions in the less synoptically forced environment of the CAPTEX 2 meteorological conditions.* Both the temporal and spatial sensitivity tests showed less overall distance error and uncertainty when HYSPLIT ingested WRF utilizing the YSU PBL scheme, as opposed to WRF with the MYNN PBL scheme. This trend points to the PBL parameterizations because this is the main difference in the parameterizations between the two WRF datasets in this study. Specifically, the MYNN scheme is a local scheme; meaning that a vertical layer within the PBL only exchanges information on the states of physical variables with its adjacent vertical layers. In contrast, the YSU scheme is a non-local scheme; meaning that communication between PBL layers is unrestricted, and one layer effectively knows the physical states of all the other layers. Other studies have shown that this allows deeper mixing of energy from the free atmosphere above the PBL into the layers within the PBL, resulting in a more realistic daytime PBL height when compared to local PBL schemes (Cohen et al. 2015). Moreover, a concurrent study found success in reducing error by optimizing the vertical turbulence and boundary layer stability parameterizations within HYSPLIT (Bazemore 2019). This further highlights the importance of representing the daytime PBL accurately for the CAPTEX releases because the first four were released during the daytime, and all of the releases in this

study spanned multiple diurnal cycles. As most of the dispersion of the plume in the CAPTEX releases occurs within the PBL, these results confirm the importance of accurately modeling this portion of the atmosphere.

Findings: NUDETs 1951-1957

This study subsequently modified the SRM methodology to a true ensemble of distinct forward HYSPLIT simulations where the source location was varied among the members. This allowed greater complexity and flexibility within the HYSPLIT configuration. Data from the nuclear detonation tests from 1951 to 1957 at the NTS were selected to model transport and dispersion of stabilized nuclear clouds in HYSPLIT and compared to observed dose rates to determine whether the detonation location could be discovered. *By iterating through multiple ensembles to narrow the search area and increase the resolution, the STE solution mean distance error was 21.8 km for the Simon case and 176.4 km for the Smoky case.* It was known from a previous study that HYSPLIT is better able to simulate the dispersion of the Simon fallout than the Smoky fallout, and this owes to the significant decrease in error with the Simon case. This is likely due to the greater vertical inhomogeneity of the Smoky meteorological conditions that featured greater vertical wind shear than the Simon meteorological conditions due to the presence of an upper level low north of the NTS. While evidence exists that the YSU PBL scheme improved the STE solutions in the CAPTEX simulations, it did not perform well in the Smoky NUDET. The PBL scheme within the WRF dictates the turbulence and vertical mixing above the PBL, so it is possible that the MYNN may improve the Smoky STE solution, as local PBL schemes like the MYNN may handle vertical wind shear more accurately as they rely on TKE fields to determine eddy mixing throughout the free atmosphere (Nolan et al. 2009; Bu et al. 2017). Further testing is required in order to determine the effect of

the vertical turbulence parameterization within the PBL scheme on the STE solution in a high wind shear environment.

In both cases, the direction of the distance error followed overall westerly flow, meaning the STE solution focused on an area to the east of both detonation locations. The methodology was able to minimize the error latitudinally in westerly flow, and struggled in the longitudinal direction. This phenomenon was also noted in the CAPTEX data. If the flow was southerly, the solution would likely contain more error in the latitudinal direction than in the longitudinal direction. Therefore, even with poor model performance, a corridor where the actual release occurred can still be identified removing one dimension from the uncertainty.

Summary

Ultimately, the acceptable level of error and uncertainty in the STE solution depends on the user and the STE problem at hand. For example, a 0.5° SRM showed consistent results with mean errors between 50-100 km and sometimes less in the CAPTEX data. This is also a computationally efficient configuration and produces a solution much faster than a 0.25° or 0.1° SRM that may not even improve the solution. If a user is trying to determine the emission of a pollutant to a certain country or region of a country, the 0.5° SRM configuration suffices. It may also suffice to confirm that the actual release occurred at a location already suspected for other reasons of being the true source. Both situations apply to nuclear treaty monitoring. On the other hand, trying to narrow down the source location to a specific city or section of a city may only be obtainable with this methodology in certain meteorological conditions with a robust observational dataset. These results provide expectations of the STE outcome given a set of meteorological conditions, data, and SRM resolution.

The following are the main takeaways of this study:

- Due to the difficulty in explicitly simulating random dispersion at higher resolutions, inputting higher resolution meteorological data and running HYSPLIT at higher resolutions does not necessarily decrease the distance error in the STE solution.

- All CAPTEX releases showed that a reliable STE solution can be obtained as long as sampling began no later than 6 hours after the actual release.

- Removing the observations nearest to the actual release location introduces the most distance error and uncertainty into the STE solution, emphasizing the importance of these observations.

- Observations surrounding or located on elevated terrain can contaminate the observational dataset as their removal prompted a decrease in the distance error of the STE solution.

- The PBL schemes utilized significantly change the STE outcome as evidenced in the CAPTEX 2 trials, even at higher resolutions.

- STE solutions can be obtained with HYSPLIT by testing source location-varying ensembles of more complex pollutant features, such as stabilized nuclear clouds.

Proposed Future Work

Expanding the cases utilized, relaxing the assumptions in Chapter III, and investigating the parameterization-driven differences in the results of Chapter IV provide the basis for future research possibilities. This study focused on CAPTEX and the NUDET cases that occurred on the mesoscale to synoptic scale. This methodology can be further tested on the mesoscale to microscale using DATEM available for

other tracer experiments, such as Metropolitan Tracer Experiment (METREX) in the vicinity of Washington, D.C. in 1984 or the Sagebrush Tracer Experiment at the Idaho National Laboratory in 2013. Also, other NUDET cases were tested in the Rolph et al. (2014) study that were not tested in this study. HYSPLIT performance metrics varied between the Simon and Smoky cases; testing other cases may yield that the mean distance error of the STE outcomes lie between the errors obtained in this study.

Additionally, assumptions made in the methodology can be changed to test their sensitivity on the STE solutions. The amount of mass and particles released at each source grid point can deviate away from the true mass that was released in the CAPTEX experiment. Also, the time of the releases with the SRM can be changed to see how accurate the actual release time estimation must be in order to still produce a reliable STE solution. Decoupling the source grid and concentration grid resolutions within the SRM can be configured to optimize solution accuracy with the precision desired by the user. For example, a 0.5° resolution concentration grid may produce the most accurate HYSPLIT simulation, but the user requires to know the source location within the resolution of a 0.25° source grid. Finally, every point on the source grid does not need to be tested, as most points yield model ranks of zero and are a waste of computational resources. Artificial intelligence and machine learning techniques could be employed to optimize which source locations should be tested given the meteorological conditions and observed data available. The multiple CAPTEX datasets provide the opportunity to train and test a neural network in order to increase the computational efficiency of this methodology.

Lastly, the results showed that improvement in the STE outcome can be obtained by selecting the optimal PBL parameterization for the meteorological model. Testing the same configuration within HYSPLIT while varying the PBL scheme utilized in

the meteorological model ingested by HYSPLIT may minimize the distance error and uncertainty across more meteorological conditions. Therefore, future work should focus on how the STE solution is sensitive to the parameterizations chosen in the meteorological model, as they are a main source of error in the STE outcome.

Appendix A: CAPTEX Sampling Sites

Site #	Location	Latitude (°N)	Longitude (°W)	Elevation (m)
302	Hundred, WV	39.65	80.42	354
304	Wheeling, WV	40.07	80.73	198
306	Steubenville, OH	40.38	80.63	303
308	Lisbon, OH	40.77	80.75	333
310	Akron-Canton, OH	40.92	81.43	369
312	Hiram, OH	41.3	81.15	375
314	Cleveland, OH	41.42	81.87	235
316	Oberlin, OH	41.3	82.22	249
318	Norwalk, OH	41.27	82.62	204
320	Fremont, OH	41.33	83.12	183
402	Somerset, PA	40	79.08	640
404	Blairsville, PA	40.43	79.15	561
406	Kittanning Lock, PA	40.82	79.53	241
408	Clarion, PA	41.2	79.43	340
410	Titusville, PA	41.63	79.7	372
412	Erie, PA	42.08	80.18	223
452	Long Point, ON	42.6	80.5	175
454	Port Stanley, ON	42.67	81.15	213
456	Wilkesport, ON	42.7	82.35	183
502	Saxton, PA	40.2	78.25	238
504	Tyrone, PA	40.67	78.23	265
506	Weedville, PA	41.3	78.48	538

Site #	Location	Latitude (°N)	Longitude (°W)	Elevation (m)
508	Bradford, PA	41.8	78.63	652
510	Little Valley, NY	42.25	78.8	480
512	Gowanda, NY	42.48	78.93	262
552	Vineland, ON	43.18	79.4	79
554	Milton, ON	43.52	79.92	221
555	Waterloo, ON	43.47	80.38	314
556	Mt. Forest, ON	43.98	80.75	415
557	Toronto, ON	43.63	79.38	77
558	CN Tower, ON	43.65	79.38	288
559	CN Tower, ON	43.65	79.38	426
602	York, PA	39.92	76.75	119
604	Newport, PA	40.48	77.13	116
606	Williamsport, PA	41.25	76.92	186
608	Westfield, PA	41.98	77.57	61
610	Haskinville, NY	42.42	77.57	500
612	Pavilion, NY	42.88	78.03	287
614	Batavia, NY	43.03	78.18	278
652	Bowmanville, ON	43.92	78.67	99
653	Peterborough, ON	44.23	78.37	191
654	Coldwater, ON	44.62	79.53	280
702	Reading, PA	40.37	75.93	82
703	Chester, NJ	40.78	74.67	289
704	Freeland, PA	41.02	75.9	580
706	Montrose, PA	41.83	75.87	475

Site #	Location	Latitude (°N)	Longitude (°W)	Elevation (m)
708	Ithaca, NY	42.45	76.45	293
710	Clyde, NY	43.07	76.83	128
752	Bloomfield, ON	43.98	77.22	91
753	Kaladar, ON	44.68	77.15	244
754	Campbellford, ON	44.28	77.78	175
756	Minden, ON	44.93	78.72	274
802	Pemberton, NJ	39.93	74.7	16
803	Wertsville, NJ	40.45	74.8	49
804	West Wharton, NJ	40.9	74.6	223
805	High Point Park, NJ	41.3	74.67	430
806	Mongaup Valley, NY	41.63	74.8	380
807	Downsville Dam, NY	42.08	74.97	396
808	Oneonta, NY	42.47	75.07	427
809	Chepachet, NY	42.92	75.12	403
810	Griffiss AFB, NY	43.23	75.4	148
811	Highmarket, NY	43.58	75.52	546
812	Watertown, NY	44	76.02	97
852	Charleston Lake, ON	44.48	76.03	92
853	Kemptville, ON	45	75.63	99
854	Golden Lake, ON	45.6	77.2	160
902	Merrick, NY	40.67	73.52	6
903	Fort Lee, NJ	40.85	73.97	70
904	Yorktown Heights, NY	41.27	73.8	204
906	Hudson Street School, NY	42.25	73.8	18

Site #	Location	Latitude (°N)	Longitude (°W)	Elevation (m)
908	Broadalbin, NY	43.05	74.2	256
910	Newcomb, NY	43.97	74.1	506
912	Norfolk, NY	44.8	75	70
952	Angers, QC	45.55	75.52	94
2	Greenport, NY	41.1	72.37	5
4	Stafford Springs, CT	41.95	72.3	139
6	Wardsboro, VT	43.03	72.8	424
8	Cornwall, VT	43.95	73.22	150
10	Ellenburg Depot, NY	44.9	73.8	262
52	Saint Hippolyte, QC	45.98	74	366
102	Providence, RI	41.73	71.43	16
104	Lawrence, MA	42.7	71.17	17
106	Mount Washington, NH	44.27	71.3	1910
107	Gorham, NH	44.4	71.18	261
108	Newport, VT	44.93	72.2	234
152	Saint Zephirin, QC	46.07	72.58	52

Table 16. The site numbers, location names, latitudes, longitudes, and elevations in meters above sea level of the sampling stations within the CAPTEX network (Ferber et al. 1986).

Appendix B: Additional CAPTEX Results

CAPTEX 5

(a)

(b)

(c)

Figure 26. Line plots for the CAPTEX 5 distance exclusion tests while utilizing (a) NARR 32.5-km, (b) WRF 27-km, and (c) WRF 9-km. The WRF meteorological files are from Ngan and Stein (2017). Data representation is identical to Figure 15.

WRF 27-KM

SRM Resolution	Hours Included After Release					
	ALL	≥6	≥12	≥18	≥24	≥36
2°	green	green	yellow	red	yellow	red
1°	green	green	green	red	red	red
0.5°	green	green	green	yellow	yellow	red
0.25°	yellow	red	red	yellow	yellow	red

WRF 9-KM

SRM Resolution	Hours Included After Release					
	ALL	≥6	≥12	≥18	≥24	≥36
2°	green	green	green	red	yellow	red
1°	green	green	green	yellow	green	red
0.5°	green	green	green	yellow	yellow	red
0.25°	yellow	yellow	red	yellow	yellow	red

NARR 32.5-KM

SRM Resolution	Hours Included After Release					
	ALL	≥6	≥12	≥18	≥24	≥36
2°	yellow	yellow	red	yellow	yellow	red
1°	green	green	green	yellow	red	red
0.5°	green	green	green	yellow	yellow	red
0.25°	yellow	yellow	green	red	yellow	red

Table 17. Reliability of the STE solution as observation times are excluded relative to the actual release time for CAPTEX 5. WRF data is from Ngan and Stein (2017). Results are color-coded according to Table 8.

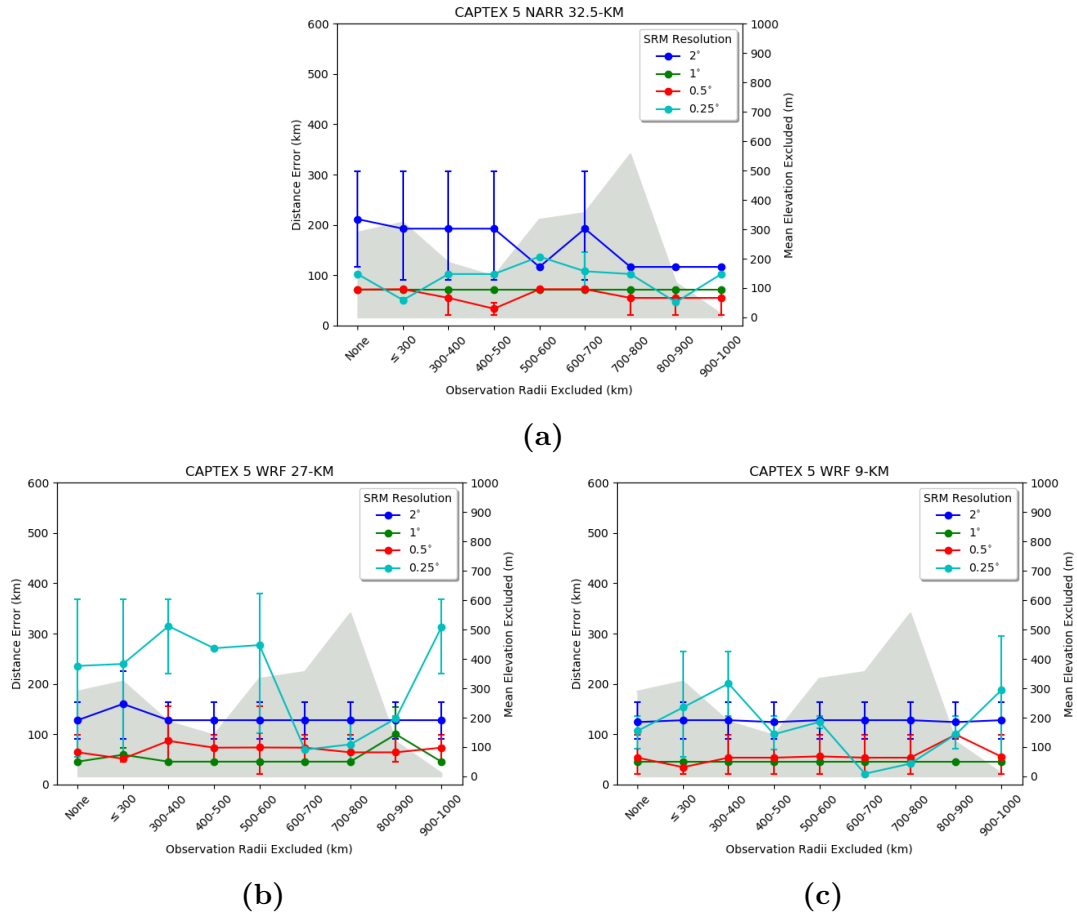# CAPTEX 7
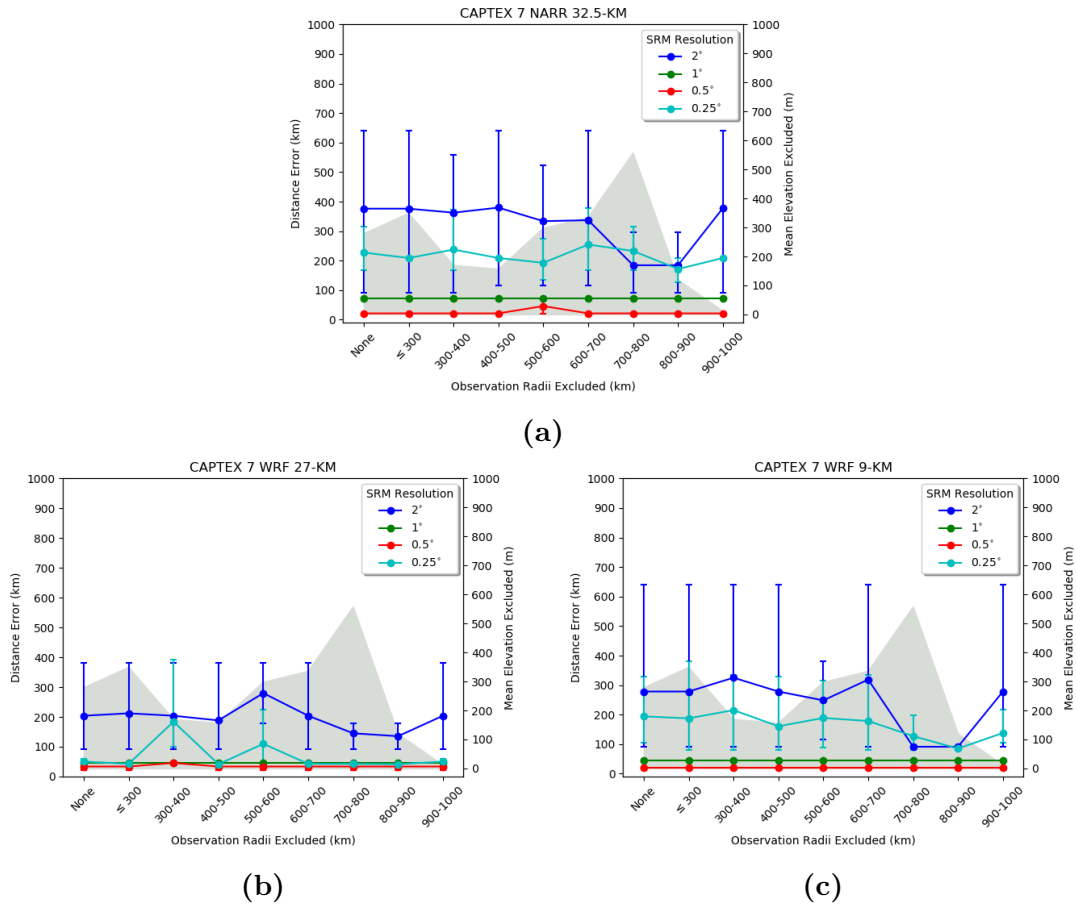

(a)

(b)

(c)

Figure 27. Line plots for the CAPTEX 7 distance exclusion tests while utilizing (a) NARR 32.5-km, (b) WRF 27-km, and (c) WRF 9-km. The WRF meteorological files are from Ngan and Stein (2017). Data representation is identical to Figure 15.

WRF 27-KM

SRM Resolution	Hours Included After Release					
	ALL	≥6	≥12	≥18	≥24	≥36
2°	yellow	yellow	yellow	yellow	red	red
1°	green	green	green	red	red	red
0.5°	green	green	green	yellow	red	yellow
0.25°	green	green	yellow	red	yellow	yellow

WRF 9-KM

SRM Resolution	Hours Included After Release					
	ALL	≥6	≥12	≥18	≥24	≥36
2°	yellow	yellow	yellow	yellow	red	red
1°	green	green	green	green	red	red
0.5°	green	green	green	yellow	red	red
0.25°	yellow	green	yellow	red	yellow	yellow

NARR 32.5-KM

SRM Resolution	Hours Included After Release					
	ALL	≥6	≥12	≥18	≥24	≥36
2°	yellow	yellow	yellow	yellow	red	red
1°	green	green	green	green	red	red
0.5°	green	green	green	green	yellow	yellow
0.25°	yellow	yellow	yellow	yellow	yellow	yellow

Table 18. Reliability of the STE solution as observation times are excluded relative to the actual release time for CAPTEX 7. WRF data is from Ngan and Stein (2017). Results are color-coded according to Table 8.

Bibliography

Air Resources Laboratory, 2018a: HYSPLIT Basic Tutorial. URL https://ready.arl. noaa.gov/documents/Tutorial/html/index.html.

Air Resources Laboratory, 2018b: HYSPLIT Workshop, College Park, MD.

Bazemore, D. W., 2019: Quantifying Uncertainty of Ensemble Transport and Dispersion Simulations Using HYSPLIT. Master's thesis, Air Force Institute of Technology, 84 pp.

Bieringer, P. E., G. S. Young, L. M. Rodriguez, A. J. Annunzio, F. Vandenberghe, and S. E. Haupt, 2017: Paradigms and Commonalities in Atmospheric Source Term Estimation Methods. *Atmospheric Environment*, **156**, 102–112, doi:10.1016/ j.atmosenv.2017.02.011, URL http://dx.doi.org/10.1016/j.atmosenv.2017.02.011.

Bu, Y. P., R. G. Fovell, and K. L. Corbosiero, 2017: The Influences of Boundary Layer Mixing and Cloud-Radiative Forcing on Tropical Cyclone Size. *Journal of the Atmospheric Sciences*, **74 (4)**, 1273–1292, doi:10.1175/JAS-D-16-0231.1, URL http://journals.ametsoc.org/doi/10.1175/JAS-D-16-0231.1.

Cohen, A. E., S. M. Cavallo, M. C. Coniglio, and H. E. Brooks, 2015: A Review of Planetary Boundary Layer Parameterization Schemes and Their Sensitivity in Simulating Southeastern U.S. Cold Season Severe Weather Environments. *Weather and Forecasting*, **30 (3)**, 591–612, doi:10.1175/WAF-D-14-00105.1, URL http:// journals.ametsoc.org/doi/10.1175/WAF-D-14-00105.1.

Draxler, R., J. Heffter, and G. Rolph, 2001: DATEM: Data Archive of Tracer Experiments and Meteorology. Tech. rep., Air Resources Laboratory, Silver Springs, MD. URL https://www.arl.noaa.gov/wp{_}arl/wp-content/uploads/documents/ datem/datem.pdf.

Draxler, R. R., 2006: The Use of Global and Mesoscale Meteorological Model Data to Predict the Transport and Dispersion of Tracer Plumes Over Washington, D.C. *Weather and Forecasting*, **21 (3)**, 383–394, doi:10.1175/WAF926.1, URL http://journals.ametsoc.org/doi/abs/10.1175/WAF926.1.

Draxler, R. R., and G. D. Hess, 1998: An Overview of the HYSPLIT_4 Modelling System for Trajectories, Dispersion, and Deposition. *Australian Meteorological Magazine*, **47 (June 1997)**, 295–308.

Draxler, R. R., and G. D. Hess, 2018: Description of the HYSPLIT_4 Modeling System. Tech. rep., Air Resources Laboratory, Silver Springs, MD. URL https://www.arl.noaa.gov/documents/reports/arl-224.pdf.

Ferber, G. J., J. L. Heffter, R. R. Draxler, R. J. Lagomarsino, F. L. Thomas, R. N. Dietz, and C. M. Benkovitz, 1986: Cross-Appalachian Tracer Experiment (CAPTEX '83) Final Report. Tech. rep., Air Reasources Laboratory, Silver Springs, MD.

Glasstone, S., and P. Dolan, 1977: The Effects of Nuclear Weapons. Tech. rep., Office of Scientific and Technical Information, Oak Ridge, TN. doi:10.2172/972902, URL http://www.osti.gov/servlets/purl/972902-YMX5Q5/.

Hutchinson, M., H. Oh, and W. H. Chen, 2017: A Review of Source Term Estimation Methods for Atmospheric Dispersion Events Using Static or Mobile Sensors. *Information Fusion*, **36**, 130–148, doi:10.1016/j.inffus.2016.11.010, URL http://dx.doi.org/10.1016/j.inffus.2016.11.010.

Ngan, F., and A. F. Stein, 2017: A Long-term WRF Meteorological Archive for Dispersion Simulations: Application to Controlled Tracer Experiments. *Journal of Applied Meteorology and Climatology*, **56 (8)**, 2203–2220, doi:10.1175/JAMC-D-16-0345.1.

Nolan, D. S., J. A. Zhang, and D. P. Stern, 2009: Evaluation of Planetary Boundary Layer Parameterizations in Tropical Cyclones by Comparison of In Situ Observations and High-Resolution Simulations of Hurricane Isabel (2003). Part I: Initialization, Maximum Winds, and the Outer-Core Boundary Layer. *Monthly Weather Review*, **137 (11)**, 3651–3674, doi:10.1175/2009MWR2785.1, URL http://journals.ametsoc.org/doi/abs/10.1175/2009MWR2785.1.

Rolph, G. D., F. Ngan, and R. R. Draxler, 2014: Modeling the Fallout from Stabilized Nuclear Clouds Using the HYSPLIT Atmospheric Dispersion Model. *Journal of Environmental Radioactivity*, **136**, 41–55, doi:10.1016/j.jenvrad.2014.05.006, URL http://dx.doi.org/10.1016/j.jenvrad.2014.05.006.

Samson, P. J., 1988: Atmospheric Transport and Dispersion of Air Pollutants Associated with Vehicular Emissions. *Air Pollution, the Automobile, and Public Health*, A. Watson, R. Bates, and D. Kennedy, Eds., National Academies Press, Washington D.C, 77–98, URL https://www.ncbi.nlm.nih.gov/books/NBK218142/?report=printable.

Seibert, P., and A. Frank, 2004: Source-Receptor Matrix Calculation with a Lagrangian Particle Dispersion Model in Backward Mode. *Atmospheric Chemistry and Physics*, **4 (1)**, 51–63, doi:10.5194/acp-4-51-2004, URL http://www.atmos-chem-phys.net/4/51/2004/.

Shankar Rao, K., 2007: Source Estimation Methods for Atmospheric Dispersion. *Atmospheric Environment*, **41 (33)**, 6964–6973, doi:10.1016/j.atmosenv.2007.04.064.

Spangler, T., 2002: Dispersion Basics. URL https://www.meted.ucar.edu/dispersion/basics/.

Stein, A. F., R. R. Draxler, G. D. Rolph, B. J. Stunder, M. D. Cohen, and F. Ngan, 2015: NOAA's HYSPLIT Atmospheric Transport and Dispersion Modeling System. *Bulletin of the American Meteorological Society*, **96 (12)**, 2059–2077, doi:10.1175/ BAMS-D-14-00110.1.

Wesely, M. L., 1989: Parameterization of Surface Resistances to Gaseous Dry Deposition in Regional-scale Numerical Models. *Atmospheric Environment*, **23 (6)**, 1295–1304, doi:10.1016/j.atmosenv.2007.10.058.

REPORT DOCUMENTATION PAGE

Form Approved
OMB No. 0704–0188

The public reporting burden for this collection of information is estimated to average 1 hour per response, including the time for reviewing instructions, searching existing data sources, gathering and maintaining the data needed, and completing and reviewing the collection of information. Send comments regarding this burden estimate or any other aspect of this collection of information, including suggestions for reducing this burden to Department of Defense, Washington Headquarters Services, Directorate for Information Operations and Reports (0704–0188), 1215 Jefferson Davis Highway, Suite 1204, Arlington, VA 22202–4302. Respondents should be aware that notwithstanding any other provision of law, no person shall be subject to any penalty for failing to comply with a collection of information if it does not display a currently valid OMB control number. **PLEASE DO NOT RETURN YOUR FORM TO THE ABOVE ADDRESS.**

1. REPORT DATE *(DD–MM–YYYY)*	2. REPORT TYPE	3. DATES COVERED *(From — To)*
21–03–2019	Master's Thesis	Oct 2017 — Mar 2019

4. TITLE AND SUBTITLE

SOURCE TERM ESTIMATION OF ATMOSPHERIC POLLUTANTS USING AN ENSEMBLE OF HYSPLIT CONCENTRATION SIMULATIONS

5a. CONTRACT NUMBER

5b. GRANT NUMBER

5c. PROGRAM ELEMENT NUMBER

6. AUTHOR(S)

Zoellick, Casey L., Captain, USAF

5d. PROJECT NUMBER

5e. TASK NUMBER

5f. WORK UNIT NUMBER

7. PERFORMING ORGANIZATION NAME(S) AND ADDRESS(ES)

Air Force Institute of Technology
Graduate School of Engineering and Management (AFIT/EN)
2950 Hobson Way
WPAFB OH 45433-7765

8. PERFORMING ORGANIZATION REPORT NUMBER

AFIT-ENP-MS-19-M-096

9. SPONSORING / MONITORING AGENCY NAME(S) AND ADDRESS(ES)

Air Force Technical Applications Center
1201 Edward H. White Ste. C-129
Patrick AFB, FL 32925
COMM 321-494-8931
Email: astrid.suarez-mullins@us.af.mil

10. SPONSOR/MONITOR'S ACRONYM(S)

AFTAC

11. SPONSOR/MONITOR'S REPORT NUMBER(S)

12. DISTRIBUTION / AVAILABILITY STATEMENT

DISTRIBUTION STATEMENT A:
APPROVED FOR PUBLIC RELEASE; DISTRIBUTION UNLIMITED.

13. SUPPLEMENTARY NOTES

14. ABSTRACT

In support of Comprehensive Nuclear-Test-Ban Treaty (CTBT) monitoring, this study works toward source term estimation (STE) of dispersive pollutants using a novel method—an ensemble of forward trajectory concentration simulations using a meteorology-coupled dispersion model. STE of a plume of atmospheric pollutants can be solved in a variety of ways, but little has been studied on the sensitivity between the horizontal resolution of the meteorology data in relation to the dispersion model and the results derived from known concentrations at multiple locations. This study tackles both these issues of resolution and observation sensitivities by employing the Hybrid Single Particle Lagrangian Integrated Trajectory (HYSPLIT) model, coupled with data from the 1983 Cross-Appalachian Tracer Experiment (CAPTEX), to determine the location of the experimental tracer releases. Furthermore, the study then applies the SRM methodology to locate the detonation location of two nuclear tests conducted in the 1950s at the Nevada Test Site (NTS). Knowing the sensitivity of the STE solution based on the number of available measurements is useful for determining the location of a release of radionuclides into the atmosphere in support of nuclear treaty monitoring.

15. SUBJECT TERMS

Atmospheric Transport and Dispersion, HYSPLIT, Source Term Estimation, CAPTEX, Stabilized Nuclear Clouds

16. SECURITY CLASSIFICATION OF:			17. LIMITATION OF ABSTRACT	18. NUMBER OF PAGES	19a. NAME OF RESPONSIBLE PERSON
a. REPORT	b. ABSTRACT	c. THIS PAGE			Maj H.R. Tseng, AFIT/ENP
U	U	U	U	115	**19b. TELEPHONE NUMBER** *(include area code)* (937) 255-3636, x4520; hsien-liang.tseng@afit.edu

Standard Form 298 (Rev. 8–98)
Prescribed by ANSI Std. Z39.18